Johann Radon Institute for
Computational and Applied Mathematics
Austrian Academy of Sciences (ÖAW)

Improved Robustness of the Fluid-Structure Interaction Simulation with a Nearly Incompressible Elasticity Model

H. Yang

RICAM-Report 2012-19

,

Improved Robustness of Fluid-Structure Interaction Simulation with a Mixed Elasticity Form in Hemodynamics

Huidong Yang[*1]

[1] Johann Radon Institute for Computational and Applied Mathematics (RICAM), Austrian Academy of Sciences, Altenbergerstrasse 69, A-4040 Linz, Austria.

Key words fluid-structure interaction, compressible and nearly incompressible elasticity, mixed displacement-pressure formulation, Newmark-β, least-square finite element stabilization, two-layer composite vessel, partitioned algorithm, Gauss-Seidel iteration, algebraic multigrid method
MSC (2010) 74F10, 65N30, 65N12, 65N55, 37M05

In this work, a nearly incompressible elasticity model coupled with an incompressible fluid model for some fluid-structure interaction (FSI) problems in hemodynamics under a three dimensional (3D) configuration is considered. A mixed displacement-pressure formulation is employed in modeling the structure, that overcomes a possible Poisson locking phenomenon. The fluid is modeled by the incompressible Navier-Stokes equations. Implicit first order methods are employed for discretizing the fluid and structure sub-problems in time: a semi-implicit Euler scheme for the fluid and a Newmark-β scheme for the structure. A proper least-square finite element stabilization parameter for the elasticity formulation depending on time discretization parameters, mesh discretization parameters and material coefficients is designed. In such a framework, an extention of the FSI problems within two-layer composite vessels is investigated. Such vessels are assumed to possess jumping material coefficients (e.g., density, Young's modulus and Poisson ratio) and to vary thicknesses from one layer to another. Numerical experiments demonstrate sensitivities of FSI solutions with respect to the material coefficients, the thicknesses of two layers, and the time discretization parameters. For solving the coupled FSI system, we employ a class of partitioned solvers which are interpreted as Gauss-Seidel iterations applied to a reduced system with fluid velocity and structure displacement unknowns on the interface only. The performance of the algorithm relying on robust and efficient algebraic multigrid methods for the fluid and structure sub-problems is studied.

1 Introduction

Numerical simulation of FSI plays important roles in hemodynamics, e.g., accurate prediction of aneurysm rupture, where both the wall stresses and fluid forces are examined; see e.g., [7, 8, 42, 49]. In hemodynamics, the blood flow is modeled by the incompressible Navier-Stokes equation under the arbitrary Lagrangian-Eulerian (ALE) framework [18, 21, 33]. For the structure, the St. Venant-Kirchhoff model (linear, isotropic, and most quite often used in the past), the neo-Hookean model, the model proposed by Wang et al. [59], and some other isotropic nonlinear hyperelastic models have been adopted. Most of these structure models are applicable to homogenous, compressible and isotropic materials, simplified for realistic arterial tissues [25, 32, 34], which are in general hyperelastic, nonhomogenous, (nearly) incompressible, and anisotropic materials. On the other hand, FSI problems in hemodynamics pose several challenges for the development of efficient and robust numerical methods due to, e.g., the so-called added-mass effect [15], the stabilized finite element discretization on moving domains [3,21,22,36,58], the large scale system of algebraic equations, the geometrical and material nonlinearities, and the strongly coupled transmission conditions. In the last decay, lots of efforts have been made on solving the coupled FSI system, e.g, the algebraic multigrid (AMG) [26, 47], preconditioned Krylov subspace [4], (Quasi-)Newton iterative [17, 20, 27, 65], and parallel domain decomposition [6, 16] methods. As observed, most of these solvers are constructed based on pure displacement formulations or (linear) compressible models for the structure sub-problems. Therefore, in our recent work [64], a mixed displacement-pressure elasticity formulation has been incorporated into a class of partitioned FSI solvers, which have demonstrated the robustness with respect to the Poisson ratio ν. In case $\nu \ll 0.5$, the simulation with the mixed displacement-pressure formulation reproduces the same FSI solution as that with a pure displacement formulation; for all range of ν, the FSI solvers show comparable performance in terms of cost and iteration numbers, including the case $\nu \to 0.5$ that usually leads to ill-conditioned system with a pure displacement formulation. As a follow-up, we refine our previous work in the following aspects.

This work was supported by the Austrian Academy of Science.
* Corresponding author: huidong.yang@oeaw.ac.at,

First of all, a Newmark-β time discretization scheme [44] is employed for discretizing the mixed structure formulation which was originally designed for the pure displacement structure formulation. The first and second order time derivatives $\dot{d}_s := \frac{\partial d_s}{\partial t}$ and $\ddot{d}_s := \frac{\partial^2 d_s}{\partial t^2}$ of the structure displacement d_s at a time level $t^{n+1} := (n+1)\delta t$, $n = 0, ...$, are accordingly discretized in the following:

$$\ddot{d}_s^{n+1} = \frac{1}{\beta \delta t^2}(d_s^{n+1} - d_s^n) - \frac{1}{\beta \delta t}\dot{d}_s^n - \frac{1-2\beta}{2\beta}\ddot{d}_s^n, \tag{1a}$$

$$\dot{d}_s^{n+1} = \dot{d}_s^n + \gamma \delta t \ddot{d}_s^{n+1} + (1-\gamma)\delta t \ddot{d}_s^n \tag{1b}$$

with the time discretization parameters $0 < \beta \leq 1$ and $0 \leq \gamma \leq 1$, where δt denotes the time step size. With a conventional Newmark scheme $2\beta = \gamma = 1$ (used in our previous work), some wiggles for the FSI solutions, e.g., the fluid pressure waves and the structure pressure waves, were observed at certain time steps and may lead to an instability in time. By raising the value of β such that $2\beta > 1$, we obtain more stable time discretization schemes without loss of accuracy.

Secondly, due to a violation of the well-known $\inf - \sup$ condition [14, 28] for equal order finite element spaces of the mixed formulation, a new least-square finite element stabilization parameter for the discretized displacement-pressure formulation using $P_1 - P_1$ finite element is proposed:

$$\tau_{s,T} := \tau_{s,T}(h_T, \delta t, \mu^l, \rho_s, \beta) = \frac{h_T^2}{2\beta\mu^l \delta t^2/\rho_s + h_T^2}, \tag{2}$$

where μ^l denotes the shear modulus, ρ_s the structure density, h_T the mesh discretization parameter. In case $\beta = 0.5$, $\tau_{s,T}$ is reduced to $\frac{h_T^2}{\mu^l \delta t^2/\rho_s + h_T^2}$. Under certain assumptions, an a priori error estimate is analyzed for such a stabilized displacement-pressure formulation. In our previous work, we used a stabilization parameter ch_T^2 with a positive constant c for the stationary case, that is not robust with respect to, e.g., the time discretization parameter δt. We expect this new designed stabilization parameter $\tau_{s,T}$, will enhance the stability of the FSI solutions.

Thirdly, we also consider FSI problems using two-layer composite vessels surrounding the fluid domain. This thanks to the fact that the mixed displacement-pressure structure model is able to represent both compressible and nearly incompressible materials in a unified way. The inner layer has common interfaces with the incompressible flow and the outer layer, respectively; while the outer lay has no common interface with the flow. Across the common interface between two layers, some material coefficients, e.g., density, Young's modulus, Poisson ratio, are jumping. We also assume varying thicknesses from one layer to another. Admittedly this composite vessel is too simple to model real tissues in hemodynamics. However, it is of particular interest to study the sensitivities of FSI solutions with respect to such a two-layer structure model, and to extend the FSI solvers for this model.

Finally, Gauss-Seidel iterations are employed to solve the reduced FSI system of two equations with fluid velocity and structure displacement unknowns on the interface only. Such a system of equations is obtained by an elimination of dual variables and remaining primal variables on the coupled FSI system. In each iteration, fluid and structure sub-problem solvers are used. In particular, a special AMG method with robust coarsening strategy for a two-layer composite structure sub-problem is highlighted.

The remainder of this paper is organized in the following way. In Section 2, we prescribe governing equations for a FSI model problem. Section 3 and Section 4 deal with time and space discretization, respectively; in particular, we analyze the stability of the structure sub-problems using the Newmark-β time integration scheme. Section 5 reinterprets a class of partitioned solvers as a Gauss-Seidel iteration applied to a reduced FSI system, and describes components of a special AMG solver for a two-layer structure model. Numerical results and detailed discussions are given in Section 6. Finally, in Section 7, we draw some conclusions, and present an outlook of future work.

2 Governing equations

The fluid sub-problem in a deformable domain $\Omega_f^t \in \mathbb{R}^3$ is governed by the incompressible Navier-Stokes equations under the ALE framework: Find the fluid velocity $u := u(x,t)$ and pressure $p_f := p_f(x,t)$ for all $x \in \Omega_f^t$ at time t such that

$$\rho_f \partial_t u|_{\mathcal{A}^t} + \rho_f((u - w_f)\cdot\nabla)u - \nabla\cdot\sigma_f(u,p_f) = 0 \quad \text{in } \Omega_f^t, \tag{3a}$$

$$\nabla\cdot u = 0 \quad \text{in } \Omega_f^t \tag{3b}$$

with Neumann boundary conditions

$$\sigma_f(u,p_f)n_f = g_{in} \quad \text{on } \Gamma_{in}^t, \tag{4a}$$

$$\sigma_f(u,p_f)n_f = 0 \quad \text{on } \Gamma_{out}^t \tag{4b}$$

on some parts of $\partial\Omega_f^t$, where ρ_f denotes the fluid density, w_f the fluid domain velocity, n_f the outward normal, $\sigma_f(u,p_f) := 2\mu\varepsilon(u) - p_f I$ the Cauchy stress tensor, $\varepsilon(u) := \frac{1}{2}(\nabla u + (\nabla u)^T)$ the strain rate tensor, μ the dynamic viscosity, and g_{in} the given data for the inflow boundary condition, $\hat{\partial}_t u|_{\mathcal{A}^t} := \partial_t u + (w_f \cdot \nabla)u$ the ALE time derivative. The ALE mapping $\mathcal{A}^t := x_0 + Ext(d_s|_{\Gamma^0})$ for all $x_0 \in \Omega_f^0$ tracks the fluid domain by $\Omega_f^t = \mathcal{A}^t(\Omega_f^0)$. A classical option for $Ext(d_s|_{\Gamma^0}) =: d_f$ is given by the harmonic extension:

$$-\Delta d_f = 0 \quad \text{in } \Omega_f^0 \tag{5}$$

with Dirichlet boundary conditions $d_f = d_s$ on Γ^0, and $d_f = 0$ on $\Gamma_{in} \cup \Gamma_{out}$. The fluid domain velocity is then given by $w_f = \frac{\partial d_f}{\partial t} \circ \mathcal{A}^{t^{-1}}$.

The structure sub-problem in a reference domain $\Omega_s^0 \in \mathbb{R}^3$ is governed by the linear elasticity equations in the Lagrangian framework: Find the structure displacement $d_s := d_s(x,t)$ and pressure $p_s := p_s(x,t)$ for all $x \in \Omega_s^0$ and time t such that

$$\begin{aligned} \rho_s \ddot{d}_s - \nabla \cdot \sigma_s(d_s, p_s) &= 0 \quad \text{in } \Omega_s^0, & \text{(6a)} \\ \nabla \cdot d_s + \vartheta p_s &= 0 \quad \text{in } \Omega_s^0 & \text{(6b)} \end{aligned}$$

with Dirichlet and Neumann boundary conditions

$$\begin{aligned} d_s &= 0 \quad \text{on } \Gamma_d^0, & \text{(7a)} \\ \sigma_s(d_s, p_s) n_s &= 0 \quad \text{on } \Gamma_n^0 & \text{(7b)} \end{aligned}$$

on respective parts of $\partial\Omega_s^0$, ρ_s denotes the structure density, n_s the outer normal, $\sigma_s(d_s) = 2\mu^l \varepsilon(d_s) - 2\mu^l p_s I$ the Cauchy stress tensor, $\mu^l := \frac{E}{2(1+\nu)}$ the Shear modulus, E the Young's modulus, $\varepsilon(d_s) = \frac{1}{2}(\nabla d_s + (\nabla d_s)^T)$ the strain rate tensor, and $\vartheta := \frac{1-2\nu}{\nu}$ an auxiliary scaling factor such that $\vartheta \to 0$ for nearly incompressible materials.

Remark 2.1 We remark, that for the two-layer composite vessels, coefficients ρ_s, μ^l, ν and ϑ are taking constant values on each layer, but may jump across the interface. We analyze the stability for the homogeneous case when these coefficients do not jump. The analysis for the case when material coefficients jump follows an analogous way.

The interface equations on $\Gamma^0 := \partial\Omega_f^0 \cup \partial\Omega_s^0$ are described by the following no-slip condition and equivalence of surface tractions, respectively:

$$\begin{aligned} u \circ \mathcal{A}^t &= \partial_t d_s \quad \text{on } \Gamma^0, & \text{(8a)} \\ \sigma_f(u, p_f) n_f \circ \mathcal{A}^t + \sigma_s(d_s, p_s) n_s &= 0 \quad \text{on } \Gamma^0. & \text{(8b)} \end{aligned}$$

3 Time discretization

For the fluid sub-problem, the semi-implicit Euler scheme is used, which leads to an Oseen type problem at each time iteration; for the structure sub-problem, the Newmark-β time integration scheme is employed. For simplicity of notations, we do not repeat boundary conditions on $\Gamma_{in/out}$ and $\Gamma_{d/n}^0$ from now on.

The time discretized fluid sub-problem reads: Find u^{n+1} and p_f^{n+1} for given u^n and w_f^n such that

$$\begin{aligned} \rho_f \delta_t u^{n+1} + \rho_f((u^n - w_f^n) \cdot \nabla) u^{n+1} - \nabla \cdot \sigma_f(u^{n+1}, p_f^{n+1}) = 0 \quad \text{in } \Omega_f^{t^n}, & \text{(9a)} \\ \nabla \cdot u^{n+1} = 0 \quad \text{in } \Omega_f^{t^n}, & \text{(9b)} \end{aligned}$$

where the backward difference operator $\delta_t(\cdot)$ is given by $\delta_t z = (z - z^n)/\delta t$.

The time discretized structure sub-problem reads: Find d_s^{n+1} and p_s^{n+1} for given d_s^n, $\dot{d}_s^n$, $\ddot{d}_s^n$ such that

$$\begin{aligned} \rho_s \delta_{tt} d_s^{n+1} - \nabla \cdot \sigma_s(d_s^{n+1}, p_s^{n+1}) = 0 \quad \text{in } \Omega_s^0, & \text{(10a)} \\ \nabla \cdot d_s^{n+1} + \vartheta p_s^{n+1} = 0 \quad \text{in } \Omega_s^0, & \text{(10b)} \end{aligned}$$

where the Newmark-β difference operator $\delta_{tt}(\cdot)$ is given by $\delta_{tt} z = \frac{1}{\beta \delta t^2}(z - d_s^n) - \frac{1}{\beta \delta t}\dot{d}_s^n - \frac{1-2\beta}{2\beta}\ddot{d}_s^n$.

In addition, the fluid and structure sub-problems are supplemented by the following transmission conditions:

$$\begin{aligned} u^{n+1} \circ \mathcal{A}^{t^n} &= \delta_t d_s^{n+1} \quad \text{on } \Gamma^0, & \text{(11a)} \\ \sigma_f(u^{n+1}, p^{n+1}) n_f \circ \mathcal{A}^{t^n} + \sigma_s(d_s^{n+1}, p_s^{n+1}) n_s &= 0 \quad \text{on } \Gamma^0, & \text{(11b)} \end{aligned}$$

which describe the Dirichlet or Neumann boundary conditions on Γ^0 for both sub-problems.

4 Space discretization

Let $H^1(\Omega_f^0)$, $H^1(\Omega_s^0)$, $L^2(\Omega_f^0)$ and $L^2(\Omega_s^0)$ denote the standard Sobolev and Lebesgue spaces [1] on Ω_f^0 and Ω_s^0, respectively. The function spaces for the fluid velocity and pressure are respectively given by $V_f^t := \{v_f : v_f \circ \mathcal{A}^t \in H^1(\Omega_f^0)^3\}$ and $Q_f^t := \{q_f : q_f \circ \mathcal{A}^t \in L^2(\Omega_f^0)\}$; the function spaces for the structure displacement and pressure are respectively prescribed by $V_s := \{v_s : v_s \in H^1(\Omega_s^0)^3\}$ and $Q_s := \{q_s : q_s \in L^2(\Omega_s^0)\}$.

4.1 Time semi-discretized weak formulations

The time semi-discretized weak formulation of the fluid sub-problem reads: Find $u^{n+1} \in V_f^t$ and $p_f^{n+1} \in Q_f^t$ such that

$$\begin{aligned} a_f(u^{n+1}, v_f) + b_f(v_f, p_f^{n+1}) &= \langle F_f^n, v\rangle, && \text{(12a)}\\ b_f(u^{n+1}, q_f) &= 0, && \text{(12b)}\end{aligned}$$

for all $v_f \in V_f^t$ and $q \in Q_f^t$, where $a_f(u,v) = (\frac{\rho_f}{\delta t}u + \rho_f((u^n - w^n)\cdot\nabla)u, v)_{\Omega_f^t} + 2\mu(\varepsilon(u), \varepsilon(v))_{\Omega_f^t}$, $b(v,q) = -(q, \nabla\cdot v)_{\Omega_f^t}$, $\langle F_f^n, v\rangle = \frac{\rho_f}{\delta t}(u^n, v)_{\Omega_f^t} + \langle g_{in}, v\rangle_{\Gamma_f^t}$.

The time semi-discretized weak formulation of the structure sub-problem reads: Find $d_s^{n+1} \in V_{s,0} := \{v \in V_s : v = 0 \text{ on } \Gamma_d^0\}$ and $p_s^{n+1} \in Q_s$ such that

$$\begin{aligned} \tilde{a}_s(d_s^{n+1}, v_s) + \tilde{b}_s(v_s, p_s^{n+1}) &= \langle \tilde{F}_s^n, v_s\rangle, && \text{(13a)}\\ \tilde{b}_s(d_s^{n+1}, q_s) - \tilde{c}_s(p_s^{n+1}, q_s) &= 0, && \text{(13b)}\end{aligned}$$

for all $v_s \in V_{s,0}$ and $q_s \in Q_s$, where $\tilde{a}_s(d,v) = \frac{\rho_s}{\beta\delta t^2}(d,v)_{\Omega_s^0} + 2\mu^l(\varepsilon(d), \varepsilon(v))_{\Omega_s^0}$, $\tilde{b}_s(v,q) = -2\mu^l(q, \nabla\cdot v)_{\Omega_s^0}$, $\tilde{c}_s(p,q) = 2\vartheta(p,q)_{\Omega_s^0}$, $\langle \tilde{F}_s^n, v\rangle = (\frac{1}{\beta\delta t^2}d_s^n + \frac{1}{\beta t}\dot{d}_s^n + \frac{1-2\beta}{2\beta}\ddot{d}_s^n, v)_{\Omega_s^0}$.

Let $H^{1/2}(\Gamma^0)$ denote the trace space of $V_{s,0}$, i.e., $H^{1/2}(\Gamma^0) = \{v_s|_{\Gamma^0} : v_s \in V_{s,0}\}$, and let $H^{-1/2}(\Gamma^0)$ be the dual space of $H^{1/2}(\Gamma^0)$. Two dual variables $\lambda_f = \sigma_f(u^{n+1}, p^{n+1})n_f \circ \mathcal{A}^{t^n}$ and $\lambda_s = \sigma_s(d_s^{n+1}, p_s^{n+1})n_s$ are introduced to represent the respective fluid and structure surface tractions on Γ^0. The weak formulation for the interface conditions reads: Find $\lambda_f \in H^{-1/2}(\Gamma^0)$ and $\lambda_s \in H^{-1/2}(\Gamma^0)$ such that

$$\begin{aligned} (u^{n+1} \circ \mathcal{A}^{t^n}, \eta)_{\Gamma^0} &= \frac{1}{\delta t}(d^{n+1} - d^n, \eta)_{\Gamma^0}, && \text{(14a)}\\ \langle \lambda_f, \eta\rangle_{\Gamma^0} &= \langle \lambda_s, \eta\rangle_{\Gamma^0}, && \text{(14b)}\end{aligned}$$

for all $\eta \in H^{1/2}(\Gamma^0)$. These two equations supplement the fully coupled FSI system by enforcing the continuity of primal variables and equivalence of dual variables on the common interface Γ^0. The complete FSI system includes (12)-(14).

4.2 Finite element discretization and stabilization

4.2.1 Stabilization for the fully discretized ALE fluid sub-problem

Let $\mathcal{T}_{f,h}$ be the triangulation of the fluid domain Ω_f^t, that is obtained by the ALE mapping of the triangulation $\mathcal{T}_{f,h}^0$ of the reference fluid domain domain Ω_f^0. The function spaces of the fluid velocity and pressure are respectively given by $V_{f,h} := \{v_f \in C^0(\overline{\Omega_f^t})^3 : v_f|_T = P_1(T)^3,\ \forall T \in \mathcal{T}_{f,h}\}$ and $Q_{f,h} := \{q_f \in C^0(\overline{\Omega_f^0}) : q_f|_T = P_1(T),\ \forall T \in \mathcal{T}_{f,h}\}$. Due to the usage of equal order interpolation spaces, the $\inf - \sup$ condition or LBB (Ladyshenskaya-Babuška-Brezzi) condition [2, 13] is violated. On the other hand, small viscosity terms or increasing the flow velocity may lead to the dominant convective transport, and hence introduces spurious oscillations. In addition, the ALE formulations on the discrete level may not exactly fulfill conservation laws, e.g, conservation of momentum. Since this is not our main focus of this work, we refer to [22, 23, 58] and the references therein.

4.2.2 Stabilization for the fully discretized structure sub-problem

For convenience of presentation, we first rescale the time semi-discretized structure sub-problem (10) in the following: Find d_s^{n+1} and p_s^{n+1} such that

$$\begin{aligned} d_s^{n+1} - 2\alpha\nabla\cdot\varepsilon(d_s^{n+1}) + 2\alpha\nabla p_s^{n+1} &= d_s^n + \delta t\dot{d}_s^n + \tfrac{(1-2\beta)\delta t^2}{2}\ddot{d}_s^n \quad \text{in } \Omega_s^0, && \text{(15a)}\\ -2\alpha(\nabla\cdot d_s^{n+1} + \vartheta p_s^{n+1}) &= 0 \quad \text{in } \Omega_s^0, && \text{(15b)}\end{aligned}$$

with a scaling factor

$$\alpha = \frac{\beta \mu^l \delta t^2}{\rho_s}. \tag{16}$$

Let $\mathcal{T}_{s,h}$ be the triangulation of the structure sub-domain Ω_s^0; let $V_{s,h} := \{v_s \in C^0(\overline{\Omega_s^0})^3 : v_s|_T = P_1(T)^3, \ \forall T \in \mathcal{T}_{s,h}\} \cap V_{s,0}$ and $Q_{s,h} := \{q_s \in C^0(\overline{\Omega_s^0}) : q_s|_T = P_1(T), \ \forall T \in \mathcal{T}_{s,h}\}$ represent the function spaces of the structure displacement and pressure, respectively.

Then the weak formulation for the structure sub-problem reads: Find $d_s^{n+1} \in V_{s,0}$ and $p_s^{n+1} \in Q_s$ such that

$$\begin{aligned} a_s(d_s^{n+1}, v_s) + b_s(v_s, p_s^{n+1}) &= \langle F_s^n, v_s \rangle, & \text{(17a)} \\ b_s(d_s^{n+1}, q_s) - c_s(p_s^{n+1}, q_s) &= 0, & \text{(17b)} \end{aligned}$$

for all $v_s \in V_{s,0}$ and $q_s \in Q_s$, where $a_s(d, v) = (d, v)_{\Omega_s^0} + 2\alpha(\varepsilon(d), \varepsilon(v))_{\Omega_s^0}$, $b_s(v, q) = -2\alpha(q, \nabla \cdot v)_{\Omega_s^0}$, $c(p, q) = 2\alpha\vartheta(p, q)_{\Omega_s^0}$, $\langle F^n, v\rangle = (d_s^n + \delta t \dot{d}_s^n + \frac{(1-2\beta)\delta t^2}{2}\ddot{d}_s^n, v)_{\Omega_s^0}$.

Remark 4.1 For simplicity, a homogeneous Neumann boundary condition on the interface Γ^0 is included in the weak form for the structure sub-problem. However, it does not affect the following analysis with other boundary conditions.

The stabilized formulation is obtained by augmenting the Galerkin discretization with the following introduced least-square finite element stabilization term:

$$-\sum_{T \in \mathcal{T}_{s,h}} \tau_{s,T}((d_{s,h}^{n+1} + 2\alpha\nabla p_{s,h}^{n+1}) - (d_{s,h}^n + \delta t \dot{d}_{s,h}^n + \frac{(1-2\beta)\delta t^2}{2}\ddot{d}_{s,h}^n), v_s + 2\alpha\nabla q_s)_T, \tag{18}$$

where $v_s \in V_{s,h}$, $q_s \in Q_{s,h}$ and $\tau_{s,T}$ is defined as in (2).

Remark 4.2 Here the second order term $-2\alpha\nabla \cdot \varepsilon(d_{s,h}^{n+1})$ vanishes elementwise since we have only considered the linear elements. An unsymmetric version of this type of stabilization (a pressure type stabilization) might be considered:

$$-\sum_{T \in \mathcal{T}_{s,h}} \tau_{s,T}((d_{s,h}^{n+1} + 2\alpha\nabla p_{s,h}^{n+1}) - (d_{s,h}^n + \delta t \dot{d}_{s,h}^n + \frac{(1-2\beta)\delta t^2}{2}\ddot{d}_{s,h}^n), 2\alpha\nabla q_s)_T. \tag{19}$$

Similar numerical results are obtained by using (18) and (19). For the analysis, we will use the symmetric form (18).

Then the stabilized mixed formulation for the structure sub-problem reads: Find $d_{s,h}^{n+1} \in V_{s,h}$ and $p_{s,h}^{n+1} \in Q_{s,h}$ such that

$$\begin{aligned} a_{s,h}(d_{s,h}^{n+1}, v_s) + b_{s,h}(v_s, p_{s,h}^{n+1}) &= \langle F_{s,h}^n, v_s \rangle, & \text{(20a)} \\ b_{s,h}(d_{s,h}^{n+1}, q_s) - c_{s,h}(p_{s,h}^{n+1}, q_s) &= \langle G_{s,h}^n, q_s \rangle, & \text{(20b)} \end{aligned}$$

for all $v_s \in V_{s,h}$ and $q_s \in Q_{s,h}$, where the bilinear and linear forms are given by $a_{s,h}(d, v) = (d, v)_{\Omega_s^0} + 2\alpha(\varepsilon(d), \varepsilon(v))_{\Omega_s^0} - \sum_{T \in \mathcal{T}_{s,h}} \tau_{s,T}(d, v)_T$, $b_{s,h}(v, q) = -2\alpha(q, \nabla\cdot v)_{\Omega_s^0} - \sum_{T \in \mathcal{T}_{s,h}} 2\tau_{s,T}\alpha(v, \nabla q)_T$, $c_{s,h}(p, q) = 2\alpha\vartheta(p, q)_{\Omega_s^0} + \sum_{T \in \mathcal{T}_{s,h}} 4\tau_{s,T}$ $\alpha^2(\nabla p, \nabla q)_T$, $\langle F_{s,h}^n, v\rangle = (d_s^n + \delta t \dot{d}_s^n + \frac{(1-2\beta)\delta t^2}{2}\ddot{d}_s^n, v)_{\Omega_s^0} - \sum_{T \in \mathcal{T}_{s,h}} 2\tau_{s,T}\alpha(d_s^n + \delta t \dot{d}_s^n + \frac{(1-2\beta)\delta t^2}{2}\ddot{d}_s^n, v)_T$, $\langle G_{s,h}^n, q\rangle =$ $-\sum_{T \in \mathcal{T}_{s,h}} 2\tau_{s,T}\alpha(d_s^n + \delta t \dot{d}_s^n + \frac{(1-2\beta)\delta t^2}{2}\ddot{d}_s^n, \nabla q)_T$.

We first make the following assumptions on the mesh discretization parameter and the scaling factor α.

Assumption 4.3 We assume that $\mathcal{T}_{s,h}$ is regular, i.e., there exists a positive constant $\overline{\sigma}$ such that for all $T \in \mathcal{T}_{s,h}$, we have $h_T/\rho_T \le \overline{\sigma}$, where h_T is the diameter of $T \in \mathcal{T}_{s,h}$ and ρ_T denotes the diameter of the inscribed ball in a $T \in \mathcal{T}_{s,h}$. Furthermore, we assume that there exists a positive constant $\underline{\sigma}$ such that for any $T \in \mathcal{T}_{s,h}$, the diameter h_T fulfills $\underline{\sigma} h \le h_T$. In addition we assume that $h < 1$.

Assumption 4.4 We assume that $\tau_{s,T}\alpha^2$ is in order of h^2, i.e., $\frac{h^2\alpha^2}{2\alpha + h^2} = \sigma h^2$, where σ is a positive constant. A simple calculation leads to $\alpha = \sqrt{\sigma h^2 + \sigma^2} + \sigma \sim \mathcal{O}(\sigma)$ when h is sufficiently small. This usually holds for the FSI simulation in the hemodynamic applications with the specified shear modulus μ^l, structure density ρ_s, and a moderate time step size δt. In such a case, $\alpha = \beta\mu^l\delta t^2/\rho_s \sim \mathcal{O}(1)$, and $\tau_{s,T}\alpha \sim \mathcal{O}(h^2)$.

For showing the stability of the mixed formulation (20), we use Verfüth's trick [54]. We first rewrite it in the following compact form (we omit the superscript $n+1$ for clarity): Find $(d_{s,h}, p_{s,h}) \in V_{s,h} \times Q_{s,h}$ such that

$$\mathcal{B}(d_{s,h}, p_{s,h}; v_s, q_s) = \mathcal{F}(v_s, q_s) \tag{21}$$

for all $(v_s, q_s) \in V_{s,h} \times Q_{s,h}$, where $\mathcal{B}(d,p;v,q) = a_{s,h}(d,v) + b_{s,h}(v,p) + b_{s,h}(d,q) - c_{s,h}(p,q)$ and $\mathcal{F}(v,q) = \langle F^n_{s,h}, v\rangle + \langle G^n_{s,h}, q\rangle$.

Some abbreviations for the norms are introduced: $\|\cdot\|_0$, $\|\cdot\|_{0,T}$ and $\|\cdot\|_1$ represent $\|\cdot\|_{L^2(\Omega^0_s)}$, $\|\cdot\|_{L^2(T)}$ and $\|\cdot\|_{H^1(\Omega^0_s)}$, respectively. An abbreviation for the seminorm is also introduced:

$$|q|_h = (\sum_{T\in\mathcal{T}_{s,h}} \tau_{s,T}\alpha^2\|\nabla q\|^2_T)^{1/2}. \tag{22}$$

Under Assumption 4.4, we observe

$$|q|_h = (\sigma \sum_{T\in\mathcal{T}_{s,h}} h^2\|\nabla q\|^2_T)^{1/2}. \tag{23}$$

With a standard scaling argument, the following estimate is obtained:

$$|q|_h \le c\|q\|_0, \quad \text{for all } q \in Q_{s,h}, \tag{24}$$

where c is a positive constant.

The boundedness of the bilinear form $\mathcal{B}$ is presented in the following Lemma.

Lemma 4.5 *Under Assumption 4.4, for all $(d,p) \in V_{s,h}\times Q_{s,h}$ and $(v,q) \in V_{s,h}\times Q_{s,h}$, there exists a positive constant c such that $\mathcal{B}(d,p;v,q) \le c(\|d\|^2_1 + (\vartheta+1)\|p\|^2_0)^{1/2}(\|v\|^2_1 + (\vartheta+1)\|q\|^2_0)^{1/2}$.*

Proof. It is easy to see $a_{s,h}(d,v) \le \|d\|_0\|v\|_0 + 2\alpha\|d\|_1\|v\|_1 + \|d\|_0\|v\|_0 \le c_1\|d\|_1\|v\|_1$. Using Assumption 4.4, $h^2 \le h$ and noticing that $h\|\nabla p\|_{0,T} \le c_2\|p\|_{0,T}$ by standard scaling argument, we obtain

$$\begin{aligned} b_{s,h}(v,p) &\le 2\alpha\|p\|_0\|v\|_1 + 2\sum_{T\in\mathcal{T}_{s,h}} h^2\|v\|_{0,T}\|\nabla p\|_{0,T} \le 2\alpha\|p\|_0\|v\|_1 + 2c_2\sum_{T\in\mathcal{T}_{s,h}} \|v\|_{0,T}\|p\|_{0,T} \\ &\le c_3(\|v\|_1\|p\|_0 + \sum_{T\in\mathcal{T}_{s,h}} \|v\|_{1,T}\|p\|_{0,T}). \end{aligned}$$

In an analogous way, $b_{s,h}(d,q) \le c_4(\|d\|_1\|q\|_0 + \sum_{T\in\mathcal{T}_{s,h}} \|d\|_{1,T}\|q\|_{0,T})$. Furthermore,

$$\begin{aligned} c_{s,h}(p,q) &\le 2\alpha\vartheta\|p\|_0\|q\|_0 + 4\sum_{T\in\mathcal{T}_{s,h}} \tau_{s,T}\alpha^2\|\nabla p\|_{0,T}\|\nabla q\|_{0,T} \\ &\le c_5\vartheta\|p\|_0\|q\|_0 + 4\sum_{T\in\mathcal{T}_{s,h}} (\sqrt{\tau_{s,T}}\alpha\|\nabla p\|_{0,T})(\sqrt{\tau_{s,T}}\alpha\|\nabla q\|_{0,T}). \end{aligned}$$

Now combing all the estimates for $a_{s,h}(d,v)$, $b_{s,h}(v,p)$, $b_{s,h}(d,q)$ and $c_{s,h}(p,q)$, and using the Schwarz inequality and the estimate (24), yields the boundedness of $\mathcal{B}$. Here c_i, $i = 1,...,4$ are positive constants. □

Next, we show the following inequality.

Lemma 4.6 *Under Assumption 4.3 and Assumption 4.4, there exist two positive constants c_1 and c_2 such that*

$$\inf_{0\neq v\in V_{s,h}} \frac{-b_{s,h}(v,p)}{\|v\|_1} \ge c_1\|p\|_0 - c_2|p|_h, \tag{25}$$

for all $p \in Q_{s,h}$.

Proof. First, it is easy to see from Lemma 5 in [64] (see also Lemma 3.3 in [24]), the following inequality holds

$$\inf_{0\neq v\in V_{s,h}} \frac{(\nabla\cdot v, p)}{\|v\|_1} \ge c_3\|p\|_0 - c_2|p|_h, \tag{26}$$

for all $p \in Q_{s,h}$. On the other hand, using Assumption 4.4, the Schwarz inequality, and (24), we have

$$\begin{aligned} \sum_{T\in\mathcal{T}_{s,h}} 2\tau_{s,T}\alpha(v,\nabla p)_T &\ge -2\sum_{T\in\mathcal{T}_{s,h}} \tau_{s,T}\alpha\|v\|_{0,T}\|\nabla p\|_{0,T} \ge -c_4 h\sum_{T\in\mathcal{T}_{s,h}} h\|v\|_{1,T}\|\nabla p\|_{0,T} \\ &\ge -c_4 h\|v\|_1(\sum_{T\in\mathcal{T}_{s,h}} h^2\|\nabla p\|^2_{0,T})^{1/2} \ge -c_5 h\|v\|_1\|p\|_0. \end{aligned} \tag{27}$$

Combining (26) and (27) yields the claim (25), when h is sufficiently small $h < \min\{1, c_3/c_5\}$. Here c_i, $i = 3,...,5$, are positive constants. □

Then the stability inequality follows.

Theorem 4.7 *Under Assumption 4.3, Assumption 4.4, and an additional assumption that the mesh size h is sufficiently small, there exists a positive constant c such that for all $(d,p) \in V_{s,h} \times Q_{s,h}$, we have*

$$\sup_{0\neq(v,q)\in V_{s,h}\times Q_{s,h}} \frac{\mathcal{B}(d,p;v,q)}{(\|v\|_1^2+(\vartheta+1)\|q\|_0^2)^{1/2}} \geq c(\|d\|_1^2+(\vartheta+1)\|p\|_0^2)^{1/2}. \tag{28}$$

P r o o f. We choose a $w \in V_{s,h}$ such that (25) is satisfied and $\|w\|_1 = \|p\|_0$. Then

$$\begin{aligned}
\mathcal{B}(d,p;-w,0) &= -a_{s,h}(d,w) - b_{s,h}(w,q) \\
&\geq -c_3\|d\|_1\|w\|_1 - \sum_{T\in\mathcal{T}_{s,h}} \frac{h^2}{2\alpha+h^2}\|d\|_1\|w\|_1 + (c_1\|p\|_0 - c_2|p|_h)\|w\|_1 \\
&\geq -c_4\|d\|_1\|p\|_0 + c_1\|p\|_0^2 - c_2|p|_h\|p\|_0 \\
&\geq -\frac{c_4}{2\gamma_1}\|d\|_1^2 + (c_1 - \frac{c_4\gamma_1}{2} - \frac{c_2\gamma_2}{2})\|p\|_0^2 - \frac{c_2}{2\gamma_2}|p|_h^2 \\
&= -c_5\|d\|_1^2 + c_6\|p\|_0^2 - c_7|p|_h^2,
\end{aligned} \tag{29}$$

where the Schwarz inequality, Lemma 4.6, and the arithmetic-geometric-mean inequality are used. On the other hand, Korn's inequality yields

$$\begin{aligned}
\mathcal{B}(d,p;d,-p) = a_{s,h}(d,d) + c_{s,h}(p,p) &= \frac{2\alpha}{2\alpha+h^2}\|d\|_0^2 + 2\alpha\|\varepsilon(d)\|_0^2 + 2\alpha\vartheta\|p\|_0^2 + 4|p|_h^2 \\
&\geq c_8(\|d\|_1^2 + \vartheta\|p\|_0^2 + |p|_h^2).
\end{aligned} \tag{30}$$

Choosing $(v,q) = (d-\delta w, -p)$, $0 < \delta < \min\{c_8/c_5, c_8/c_7\}$, and using (29), (30), we now obtain

$$\begin{aligned}
\mathcal{B}(d,p;v,q) = \mathcal{B}(d,p;d-\delta w,-p) &= \mathcal{B}(d,p;d,-p) + \delta\mathcal{B}(d,p;-w,0) \\
&\geq (c_8-\delta c_5)\|d\|_1^2 + (\delta c_6 + c_8\vartheta)\|p\|_0^2 + (c_8-\delta c_7)|p|_h^2 \\
&\geq c_9(\|d\|_1^2 + (\vartheta+1)\|p\|_0^2).
\end{aligned} \tag{31}$$

Furthermore it is easy to see

$$\begin{aligned}
\|v\|_1^2 + (\vartheta+1)\|q\|_0^2 = \|d-\delta w\|_1^2 + (\vartheta+1)\|p\|_0^2 &\leq 2\|d\|_1^2 + 2\delta^2\|w\|_1^2 + (\theta+1)\|p\|_0^2 \\
&= 2\|d\|_1^2 + (2\delta^2+\theta+1)\|p\|_0^2 \leq c_{10}(\|d\|_1^2 + (\vartheta+1)\|p\|_0^2).
\end{aligned} \tag{32}$$

Combing (31) and (32) yields (34). Here c_i, $i = 1, ..., 10$ are positive constants, and γ_1, γ_2 are sufficiently small positive constants. □

The existence and uniqueness of the discrete structure sub-problem (20) immediately follows from Lemma 4.5 and Theorem 4.7. Now following the argument for the proof of Theorem 3.1 in [24], the a priori error estimate yields.

Theorem 4.8 *Assuming the solution (d_s, p_s) to (17) fulfills $d_s \in H_2(\Omega_s^0)^3$ and $p_s \in H_1(\Omega_s^0)$, then the discrete solution $(d_{s,h}, p_{s,h})$ to (20) satisfies the following discretization error estimate*

$$\|d_s - d_{s,h}\|_1 + \|p_s - p_{s,h}\|_0 \leq ch(\|d_s\|_2 + \|p_s\|_1) \tag{33}$$

with a positive constant c.

4.2.3 Some remarks on two-layer composite vessels

For two-layer composite vessels, following the same techniques, we have the following results for the boundedness and stability, respectively.

Lemma 4.9 *Under Assumption 4.4, for all $(d,p) \in V_{s,h}\times Q_{s,h}$ and $(v,q) \in V_{s,h}\times Q_{s,h}$, there exists a positive constant c such that $\mathcal{B}(d,p;v,q) \leq c(\|d\|_1^2 + (\overline{\vartheta}+1)\|p\|_0^2)^{1/2}(\|v\|_1^2 + (\overline{\vartheta}+1)\|q\|_0^2)^{1/2}$, where $\overline{\vartheta}$ denotes the maximum of ϑ from two structure layers.*

Theorem 4.10 *Under Assumption 4.3, Assumption 4.4, and an additional assumption that the mesh size h is sufficiently small, there exists a positive constant c such that for all $(d,p) \in V_{s,h} \times Q_{s,h}$, we have*

$$\sup_{0\neq(v,q)\in V_{s,h}\times Q_{s,h}} \frac{\mathcal{B}(d,p;v,q)}{(\|v\|_1^2 + (\underline{\vartheta}+1)\|q\|_0^2)^{1/2}} \geq c(\|d\|_1^2 + (\underline{\vartheta}+1)\|p\|_0^2)^{1/2}, \tag{34}$$

where $\underline{\vartheta}$ denotes the minimum of ϑ from two structure layers.

Then for such a two-layer structure model, we obtain the same a priori error estimate as in Theorem 4.8.

4.2.4 Finite element discretization for the interface equations

The dual variables λ_f and λ_s are discretized by mortar finite element methods, using the space of Lagrange multipliers [9] or the dual space of Lagrange multipliers [61], which will give rise to mass matrices or diagonal matrices assembled from the interface Γ^0, respectively. In this work, for simplicity, we assume a matching interface grid such that the same mass or diagonal matrices are obtained from both mortar and non-mortar sides. However, the methodology is still applicable in case of non-matching grids.

5 Strategies on solving the coupled FSI system

5.1 A class of FSI solvers using Gauss-Seidel iterations

Two fundamental approaches, the monolithic and the partitioned, are often used for solving the coupled FSI system; see e.g., [4,5,26,31,38,39,41,43,60]. The monolithic approach is considered to be more robust than its partitioned counterpart, in which the coupled system of nonlinear algebraic equations is solved as a whole. However the partitioned approach can take more advantages of software modularity, in which the fluid and the structure sub-problems are coupled via a fixed point iteration. Since some efficient and robust solvers for sub-problems, e.g., AMG methods [37,56,57,62,64,65], are available to us, the partitioned approach will be adopted in this work. We reinterpret the algorithm as a Gauss-Seidel iteration applied to a reduced system with fluid velocity and structure displacement unknowns on the interface only.

5.1.1 A Dirichlet-Neumann iteration

The coupled FSI system arises from the time-space discretization:

$$\left[\begin{array}{cc|cc|cc} Y_{ff} & Y_{f\Gamma} & 0 & 0 & 0 & 0 \\ Y_{\Gamma f} & Y_{\Gamma\Gamma} & 0 & 0 & -M_\Gamma & 0 \\ \hline 0 & 0 & X_{\Gamma\Gamma} & X_{\Gamma s} & 0 & -M_\Gamma \\ 0 & 0 & X_{s\Gamma} & X_{ss} & 0 & 0 \\ \hline 0 & M_\Gamma & -\frac{1}{\delta t}M_\Gamma & 0 & 0 & 0 \\ 0 & 0 & 0 & 0 & M_\Gamma & M_\Gamma \end{array}\right] \left[\begin{array}{c} V_f \\ V_\Gamma \\ D_\Gamma \\ D_s \\ \Lambda_f \\ \Lambda_s \end{array}\right] = \left[\begin{array}{c} F_f \\ F_{f\Gamma} \\ F_{s\Gamma} \\ F_s \\ -\frac{1}{\delta t}M_\Gamma D_\Gamma^n \\ 0 \end{array}\right], \tag{35}$$

where the first and the second parts correspond to the fluid and the structure sub-problems with homogeneous Neumann boundary conditions on Γ^0, respectively. The unique solvability of the coupled system is then guaranteed by enforcing the interface conditions as the third part. The notations of matrices and degrees of freedom (Dofs) are listed in the following:

V_Γ/V_f : Dofs of velocity on Γ^0/the remaining,	$Y_{ff},\ Y_{f\Gamma},\ Y_{\Gamma f},\ Y_{\Gamma\Gamma}$: fluid stiffness matrices ,
D_Γ/D_s : Dofs of displacement on Γ^0/the remaining,	$X_{ss},\ X_{s\Gamma},\ X_{\Gamma s},\ X_{\Gamma\Gamma}$: structure stiffness matrices,
$\Lambda_f/\ \Lambda_s$: Dofs of λ_f and λ_s on Γ^0,	M_Γ : mass matrix on Γ^0.

The reinterpretation of the partitioned approach is based on the following reduced system of (35):

$$\left[\begin{array}{cc} I & -\frac{1}{\delta t}I \\ S_f & S_s \end{array}\right] \left[\begin{array}{c} V_\Gamma \\ D_\Gamma \end{array}\right] = \left[\begin{array}{c} -\frac{1}{\delta t}D_\Gamma^n \\ H_f + H_s \end{array}\right], \tag{36}$$

where $S_f = Y_{\Gamma\Gamma} - Y_{\Gamma f}Y_{ff}^{-1}Y_{f\Gamma}$ and $S_s = X_{\Gamma\Gamma} - X_{\Gamma s}X_{ss}^{-1}X_{s\Gamma}$ are the fluid and structure Schur complements mapping the Dirichlet data to the Neumann data, respectively, $H_f = F_{f\Gamma} - Y_{\Gamma f}Y_{ff}^{-1}F_f$ and $H_s = F_{s\Gamma} - X_{\Gamma s}X_{ss}^{-1}F_s$. A Gauss-Seidel iteration applied to (36) corresponds to the following steps:

Algorithm 1 A Gauss-Seidel iteration on system (36)

For given D_Γ^k, $k \geq 0$,
1. $V_\Gamma^{k+1} = -\frac{1}{\delta t} D_\Gamma^n + \frac{1}{\delta t} D_\Gamma^k$,
2. $D_\Gamma^{k+1} = S_s^{-1}(H_f + H_s - S_f V_\Gamma^{k+1})$.

The above Gauss-Seidel iteration is nothing but a Richardson iteration applied to the system (36):

$$\begin{bmatrix} V_\Gamma^{k+1} \\ D_\Gamma^{k+1} \end{bmatrix} = \begin{bmatrix} V_\Gamma^{k} \\ D_\Gamma^{k} \end{bmatrix} + P_L^{-1} \left(\begin{bmatrix} -\frac{1}{\delta t} D_\Gamma^n \\ H_f + H_s \end{bmatrix} - \begin{bmatrix} I & -\frac{1}{\delta t} I \\ S_f & S_s \end{bmatrix} \begin{bmatrix} V_\Gamma^{k} \\ D_\Gamma^{k} \end{bmatrix} \right) \tag{37}$$

with a left preconditioner $P_L = \begin{bmatrix} I & 0 \\ S_f & S_s \end{bmatrix}$. Each Gauss-Seidel iteration requires solving a fluid Dirichlet sub-problem (S_f) and a structure Neumann sub-problem (S_s^{-1}), which is a classical Dirichlet-Neumann (DN) iteration in the FSI solver. It is equivalent to the following Richardson iteration:

$$D_\Gamma^{k+1} = D_\Gamma^k + P_L^{-1}(H_f + H_s + \tilde{S}_f D_\Gamma^n - (\tilde{S}_f + S_s) D_\Gamma^k) \tag{38}$$

applied to the Schur complement equation of (35):

$$(\tilde{S}_f + S_s) D_\Gamma = H_f + H_s + \tilde{S}_f D_\Gamma^n \tag{39}$$

with $\tilde{S}_f = \frac{1}{\delta t} S_f$ and a left preconditioner $P_L = S_s$ that is assumed to dominate the iteration. In order to accelerate the convergence rate of the DN iterations, a relaxation method, e.g., Aitken relaxation [39], may be considered.

Remark 5.1 For nonmatching interface grids, the mass matrices $M_{s\Gamma}$ and $M_{f\Gamma}$ arising from the mortar finite element discretization for fluid and structure sides, will be different. However, one of them is still invertible. Thus the Gauss-Seidel iteration in Algorithm 1 is still applicable.

5.1.2 A Robin-Robin iteration

As in domain decomposition (DD) community [46, 50], the interface condition (8) is sometimes replaced by an equivalent Robin-Robin (RR) type transmission condition with weighted Dirichlet and Neumann contributions. A proper choice of weighting parameters yields an optimal convergence rate. For this particular FSI problem, the RR condition [64] is prescribed by

$$\alpha_f u \circ \mathcal{A}^t + \sigma_f(u, p_f) n_f \circ \mathcal{A}^t = \alpha_f \partial_t d_s - \sigma_s(d_s, p_s) n_s \quad \text{on } \Gamma^0, \tag{40a}$$

$$\alpha_s \partial_t d_s + \sigma_s(d_s, p_s) n_s = \alpha_s u \circ \mathcal{A}^t - \sigma_f(u, p_f) n_f \circ \mathcal{A}^t \quad \text{on } \Gamma^0, \tag{40b}$$

where the weighting parameters α_f and α_s are positive constants. The time-space discretized FSI system with such a RR condition then follows

$$\left[\begin{array}{cc|cc|cc} Y_{ff} & Y_{f\Gamma} & 0 & 0 & 0 & 0 \\ Y_{\Gamma f} & Y_{\Gamma\Gamma} & 0 & 0 & -M_\Gamma & 0 \\ \hline 0 & 0 & X_{\Gamma\Gamma} & X_{\Gamma s} & 0 & -M_\Gamma \\ 0 & 0 & X_{s\Gamma} & X_{ss} & 0 & 0 \\ \hline 0 & \alpha_f M_\Gamma & -\frac{\alpha_f}{\delta t} M_\Gamma & 0 & M_\Gamma & M_\Gamma \\ 0 & -\alpha_s M_\Gamma & \frac{\alpha_s}{\delta t} M_\Gamma & 0 & M_\Gamma & M_\Gamma \end{array}\right] \left[\begin{array}{c} V_f \\ V_\Gamma \\ D_\Gamma \\ D_s \\ \Lambda_f \\ \Lambda_s \end{array}\right] = \left[\begin{array}{c} F_f \\ F_{f\Gamma} \\ F_{s\Gamma} \\ F_s \\ -\frac{\alpha_f}{\delta t} M_\Gamma D_\Gamma^n \\ \frac{\alpha_s}{\delta t} M_\Gamma D_\Gamma^n \end{array}\right]. \tag{41}$$

Remark 5.2 The above system (41) is actually a preconditioned system of (35) with a left preconditioner

$$P_L = \left[\begin{array}{cc|cc|cc} I & 0 & 0 & 0 & 0 & 0 \\ 0 & I & 0 & 0 & 0 & 0 \\ \hline 0 & 0 & I & 0 & 0 & 0 \\ 0 & 0 & 0 & I & 0 & 0 \\ \hline 0 & 0 & 0 & 0 & \frac{1}{\alpha_f - \alpha_s} I & -\frac{1}{\alpha_f - \alpha_s} I \\ 0 & 0 & 0 & 0 & \frac{\alpha_s}{\alpha_s - \alpha_f} I & -\frac{\alpha_f}{\alpha_s - \alpha_f} I \end{array}\right].$$

From the fluid and structure parts of (41), we obtain:

$$\begin{aligned} M_\Gamma \Lambda_f &= S_f V_\Gamma - H_f, \\ M_\Gamma \Lambda_s &= S_s D_\Gamma - H_s. \end{aligned}$$

A reduced system of (41) with fluid domain velocity and structure displacement unknowns on Γ^0 then follows:

$$\left[\begin{array}{cc} S_f + \alpha_f M_\Gamma & S_s - \frac{\alpha_f}{\delta t} M_\Gamma \\ S_f - \alpha_s M_\Gamma & S_s + \frac{\alpha_s}{\delta t} M_\Gamma \end{array} \right] \left[\begin{array}{c} V_\Gamma \\ D_\Gamma \end{array} \right] = \left[\begin{array}{c} H_f + H_S - \frac{\alpha_f}{\delta t} M_\Gamma D_\Gamma^n \\ H_f + H_s + \frac{\alpha_s}{\delta t} M_\Gamma D_\Gamma^n \end{array} \right], \tag{42}$$

for which we apply the following Gauss-Seidel iteration:

Algorithm 2 A Gauss-Seidel iteration on system (42)

For given D_Γ^k, $k \geq 0$,
1. $V_\Gamma^{k+1} = (S_f + \alpha_f M_\Gamma)^{-1}(H_f + H_s - \frac{\alpha_f}{\delta t} M_\Gamma D_\Gamma^n - (S_s - \frac{\alpha_f}{\delta t} M_\Gamma) D_\Gamma^k)$,
2. $D_\Gamma^{k+1} = (S_s + \frac{\alpha_s}{\delta t} M_\Gamma)^{-1}(H_f + H_s + \frac{\alpha_s}{\delta t} M_\Gamma D_\Gamma^n - (S_f - \alpha_s M_\Gamma) V_\Gamma^{k+1})$.

It is easy to see the above Gauss-Seidel iteration corresponds to a Richardson iteration applied to the system (42):

$$\left[\begin{array}{c} V_\Gamma^{k+1} \\ D_\Gamma^{k+1} \end{array} \right] = \left[\begin{array}{c} V_\Gamma^{k} \\ D_\Gamma^{k} \end{array} \right] + P_L^{-1} \left(\left[\begin{array}{c} H_f + H_s - \frac{\alpha_f}{\delta t} M_\Gamma D_\Gamma^n \\ H_f + H_s + \frac{\alpha_s}{\delta t} M_\Gamma D_\Gamma^n \end{array} \right] - \left[\begin{array}{cc} S_f + \alpha_f M_\Gamma & S_s - \frac{\alpha_f}{\delta t} M_\Gamma \\ S_f - \alpha_s M_\Gamma & S_s + \frac{\alpha_s}{\delta t} M_\Gamma \end{array} \right] \left[\begin{array}{c} V_\Gamma^k \\ D_\Gamma^k \end{array} \right] \right) \tag{43}$$

with a left preconditioner $P_L = \left[\begin{array}{cc} S_f + \alpha_f M_\Gamma & 0 \\ S_f - \alpha_s M_\Gamma & S_s + \frac{\alpha_s}{\delta t} M_\Gamma \end{array} \right]$. Each Gauss-Seidel iteration requires solving a structure Dirichlet sub-problem (S_s), a fluid Robin sub-problem ($(S_f + \alpha_f M_\Gamma)^{-1}$), and a structure Robin sub-problem ($(S_s + \frac{\alpha_s}{\delta t} M_\Gamma)^{-1}$). It is a reinterpretation of the corresponding three steps in Section 3.3 of [64] which are based on an iteration procedure applied to the whole coupled RR FSI system (41). In fact, from the Gauss-Seidel iteration, it follows:

$$D_\Gamma^{k+1} = D_\Gamma^k + (\alpha_f + \alpha_s)(S_s + \frac{\alpha_s}{\delta t} M_\Gamma)^{-1} M_\Gamma (S_f + \alpha_f M_\Gamma)^{-1}(H_f + H_s + \frac{1}{\delta t} S_f D_\Gamma^n - (\frac{1}{\delta t} S_f + S_s) D_\Gamma^k),$$

which is nothing but a Richardson iteration:

$$D_\Gamma^{k+1} = D_\Gamma^k + P_L^{-1}(H_f + H_s + \tilde{S}_f D_\Gamma^n - (\tilde{S}_f + S_s) D_\Gamma^k) \tag{44}$$

applied to the Schur complement equation (39), with a left preconditioner $P_L = \frac{1}{\alpha_f + \alpha_s}(S_f + \alpha_f M_\Gamma) M_\Gamma^{-1}(S_s + \frac{\alpha_s}{\delta t} M_\Gamma)$. In case $\alpha_s = 0$, a Robin-Neumann (RN) preconditioner $P_L = \frac{1}{\alpha_f}(S_f + \alpha_f M_\Gamma) M_\Gamma^{-1} S_s$ is obtained; in case $\alpha_f = \infty$, $\alpha_s = 0$, a conventional DN preconditioner $P_L = S_s$ is obtained. In order to accelerate the convergence rate, a Krylov sub-space method (e.g., the GMRES method [48] or the BiCGstab method [53] due to the unsymmetric system) may be applied to the reduced systems (36) and (42). From a memory consumption point of view, a more effective way is to combine a proper preconditioner, e.g. RN, with the GMRES method on the further reduced FSI system (39). In this work, the RN preconditioned GMRES method is employed to solve all numerical tests.

5.2 Robust AMG methods

5.2.1 An AMG method for the fluid sub-problem

Fast solvers for solving the discretized (linearized) Navier-Stokes equations arising from the fluid sub-problem have been studied continuously; see, e.g., [10, 11, 19, 30, 35, 45, 52]. A special AMG method for the $P_1 - P_1$ stabilized finite element discretization of the Navier-Stokes equations has been studied by M. Wabro [56, 57]. Unlike in geometrical multigrid (GMG) methods [29, 51], where the mesh discretization on coarse levels is available and $\inf - \sup$ stable saddle point systems are constructed easily, in AMG method, a special care for the discrete $\inf - \sup$ condition on coarse levels has to be taken into account since we have no access to meshes on coarse levels. In our previous work [62, 65], we extended the stabilized AMG coarsening strategy for solving the discretized fluid sub-problems on general hybrid meshes. Due to its robustness and efficiency, such an AMG method is used to solve the fluid sub-problem in this work.

5.2.2 An extension of an AMG method for the two-layer structure sub-problem

The stabilized AMG coarsening strategy for the structure sub-problem covering both compressible and nearly incompressible models on general hybrid meshes, has been investigated in [64]. As a continuation of the previous work, we extend this approach to a two-layer structure sub-problem.

Let us first reorder the saddle point system of equations for the structure sub-problem, such that we have degrees of freedom of the displacement in the first place, and the pressure in the second place:

$$K \begin{bmatrix} d \\ p \end{bmatrix} = \begin{bmatrix} f \\ g \end{bmatrix} \text{ with } K := \begin{bmatrix} A & B^T \\ B & -C \end{bmatrix},$$

where each block of K has a structure which couples the degrees of freedom from two layers, e.g., $A = \begin{bmatrix} A_{11} & A_{1\Gamma} & 0 \\ A_{\Gamma 1} & A_{\Gamma\Gamma} & A_{\Gamma 2} \\ 0 & A_{2\Gamma} & A_{22} \end{bmatrix}$ couples the degrees of freedom in each layer and on the interface between two layers by $A_{1\Gamma}/A_{\Gamma 1}$ and $A_{2\Gamma}/A_{\Gamma 2}$.

We construct the prolongation operator from the coarse level $l+1$ to the next finer level l in a block-diagonal matrix form:

$$P_{l+1}^l : \begin{bmatrix} (\mathbb{R}^3)^{m_{l+1}} \\ \mathbb{R}^{m_{l+1}} \end{bmatrix} \longrightarrow \begin{bmatrix} (\mathbb{R}^3)^{m_l} \\ \mathbb{R}^{m_l} \end{bmatrix}, \; P_{l+1}^l = \begin{bmatrix} I_{l+1}^l & 0 \\ 0 & J_{l+1}^l \end{bmatrix},$$

where m_l is the number of pressure (or one component of displacement) degrees of freedom on the level l, I_{l+1}^l and J_{l+1}^l are prolongation matrices for the displacement and pressure, respectively.

For the restriction from the finer level l to the next coarser level $l+1$ we choose the transposed matrix:

$$R_l^{l+1} = (P_{l+1}^l)^T = \begin{bmatrix} I_l^{l+1} & 0 \\ 0 & J_l^{l+1} \end{bmatrix},$$

where $I_l^{l+1} = (I_{l+1}^l)^T$ and $J_l^{l+1} = (J_{l+1}^l)^T$. The system matrix on the level l has a form $K_l = \begin{bmatrix} A_l & B_l^T \\ B_l & -C_l \end{bmatrix}$. Then on the next coarser level $l+1$, the system matrix is obtained by a modified Galerkin projection method:

$$K_{l+1} = R_l^{l+1} K_l P_{l+1}^l = \begin{bmatrix} A_{l+1} & B_{l+1}^T \\ B_{l+1} & -C_{l+1} \end{bmatrix}$$

with $A_{l+1} = I_l^{l+1} A_l I_{l+1}^l$, $B_{l+1} = J_l^{l+1} B_l I_{l+1}^l$, $C_{l+1} = \tilde{M}_{l+1} + \frac{\lambda_{\max}(D_l^{-1} M_l)}{h^2} \tilde{C}_{l+1}$, where $\tilde{M}_{l+1}$ and $\tilde{C}_{l+1}$ correspond to the pressure mass matrix scaled with the parameter ϑ and the pressure stabilization matrix, respectively, obtained by standard Galerkin projection on level $l+1$. The matrix D_l denotes the diagonal of A_l, and M_l the mass matrix in the displacement space. Then under appropriate assumptions on the mesh, we obtain the following stability results on all coarse levels:

Theorem 5.3 *For each coarse level $l = \{2, ..., L\}$, there is a positive constant ζ_l such that*

$$\sup_{0 \neq (\underline{v}, \underline{q}) \in \underline{V}_l \times \underline{Q}_l} \frac{\mathcal{B}_l((\underline{d}, \underline{p}), (\underline{v}, \underline{q}))}{\|\underline{v}\|_{A_l} + (1+\underline{\vartheta})\|\underline{q}\|_{M_l}} \geq \zeta_l \left(\|\underline{d}\|_{A_l} + (1+\underline{\vartheta})\|\underline{p}\|_{M_l} \right) \tag{45}$$

for all $(\underline{d}, \underline{p}) \in \underline{V}_l \times \underline{Q}_l := (\mathbb{R}^3)^{m_l} \times \mathbb{R}^{m_l}$, where $\|\underline{v}\|_{A_l} = \underline{v}^T A_l \underline{v}$, $\|\underline{q}\|_{M_l} = \underline{q}^T M_l \underline{q}$, and

$$\mathcal{B}_l((\underline{d}, \underline{p}), (\underline{v}, \underline{q})) = \underline{v}^T A_l \underline{d} + \underline{v}^T B_l^T \underline{p} + \underline{q}^T B_l \underline{d} - \underline{q}^T C_l \underline{p}.$$

P r o o f. We first prove an inequality similar to (25) with discrete norms on all coarse levels using an induction:

$$\sup_{0 \neq v \in \underline{V}_l} \frac{v B_l^T p}{\|v\|_{A_{D_l}}} \geq c_1 \|p\|_{M_l} - c_2 (p^T C_l p)^{1/2} \text{ for all } p \in \underline{Q}_l$$

with positive constants c_1 and c_2. Then following the strategy showing the stability of the two-layer structure sub-problem on the continuous level, the stability with discrete norms on all levels yields. For details, we refer to [55, 62] for the Stokes problem, and [64] for the nearly incompressible elasticity problem, which follow the same procedure. □

Here for a level $l \in \{2, ..., L\}$, $\underline{V}_l$ and $\underline{Q}_l$ represent the spaces of the coefficient vectors corresponding to the proper displacement and pressure finite element spaces on level l, respectively.

For a smoothing procedure, we use a Braess-Sarazin-type smoother [12, 66], which is a preconditioned Richardson method:

$$\begin{bmatrix} d^{k+1} \\ p^{k+1} \end{bmatrix} = \begin{bmatrix} d^k \\ p^k \end{bmatrix} + \hat{K}^{-1} \begin{bmatrix} f - Ad^k - B^T p^k \\ g - Bd^k + Cp^k \end{bmatrix}$$

with a symmetric and indefinite preconditioner $\hat{K} = \begin{bmatrix} \hat{A} & B^T \\ B & \hat{A}^{-1}B^T - \hat{S} \end{bmatrix}$, where as suggested in [55], we use $\hat{A} = 2diag(A)$, and thus $\hat{S} = C + \frac{1}{2}B^T(diag(A))^{-1}B$. One step of this method requires us to solve the following three equations consecutively: $\hat{A}(\hat{d}^{k+1} - d^k) = f - Ad^k - B^T p^k$, $\hat{S}(p^{k+1} - p^k) = B\hat{d}^{k+1} - Cp^k - g$, and $\hat{A}(d^{k+1} - d^k) = -B^T(p^{k+1} - p^k)$. As suggested in [66], a more efficient Braess-Sarazin smoother requires an approximate solution of the pressure correction equation obtained by applying an (inner) AMG method with starting value 0 to solve this equation approximately.

6 Results and discussions

6.1 FSI results with a homogeneous structure model

For a comparison, we use the same benchmark as in [64], which is quite often used by many others; see e.g., [17,20,26,27]. Note that in many papers, the Centimetre Gram Second (CGS) physical units are adopted, as opposed to the International System of Units (SI units) used in [64]. However, both quantities are equivalent in case of compressible material; see Table 1 for the qualities measured by CGS units and SI units (in brackets) . In this work, we stick to the CGS units. We also point out that in many papers, only the compressible elasticity model with a pure displacement formulation is reported; while the FSI simulation with both compressible and nearly incompressible structure models is considered in [64].

Fluid	Structure
$\rho_f = 1.0$ g/cm^3	$\rho_f = 1.2$ g/cm^3
$\mu = 0.03$ Poise (0.003 Pa·s)	$E = 2.9908 \times 10^6$ dyn/cm^2 (29.908 N/cm^2)
$g_{in} = (0, 0, 0.1332)^T$ N/cm^2 ($(0, 0, 1.332 \times 10^4)^T$ dyn/cm^2) if $t \leq 3$ ms $g_{in} = 0$ dyn/cm^2 (0 N/cm^2) if $t > 3$ ms	$\nu = 0.3003$ (compressible) $\nu = 0.499999$ (nearly incompressible)

Table 1 The values of fluid and structure material coefficients and fluid inflow boundary conditions.

The FSI simulation is performed on a cylindrical vessel filled with fluid. The computational fluid domain has length 50 mm in the z-direction and radius 5 mm, surrounded by the structure body with the thickness 1 mm. The time step size is set as $\delta t = 0.0625$ ms. We run the simulation until $t = 10$ ms. The mesh contains $17,904$ nodes and $17,489$ tetrahedral elements ($7,434$ structure elements and $10,055$ fluid elements). The overall degrees of freedom is about $70,000$. For a comparison, we pick up a point PtA (with a coordinate $[0, 0, 25]$ mm) in the middle of the center line of the fluid domain, and a point PtB (with a coordinate $[0, 5, 25]$ mm) near the moving interface (see black dots in Fig. 1 for an illustration). We record the fluid pressure values along the time at these two points, and plot the values as functions of time t.

Note that in the following figures, without particular specification, the horizontal axis represents the simulating time measured in Millisecond (ms); the fluid pressure value is plotted in the vertical direction.

6.1.1 A compressible case: $\nu = 0.3003$

We first test a benchmark with a compressible material, using different choices of time discretization parameters $\beta = 0.5$, 0.625, and $\gamma = 1.0$. Note that in [64], we were using $\beta = 0.5$, $\gamma = 1.0$, and a simple stabilization parameter in order of h^2. Here we are able to choose different combinations of time discretization parameters β, γ, and to use a more robust stabilization parameter $\tau_{s,T}$. The numerical results are comparable to each other; see Fig. 2.

6.1.2 A nearly incompressible case: $\nu = 0.499999$

For a nearly incompressible material, the method we used in [64] may lead to some wiggles if the mesh size is not sufficient fine with respect to the time step size. There might be two reasons for this: First of all, the choice of $\beta = 0.5$ and $\gamma = 1.0$ in the mixed elasticity form is not as good as in the pure displacement form; secondly, the stabilization parameter we used

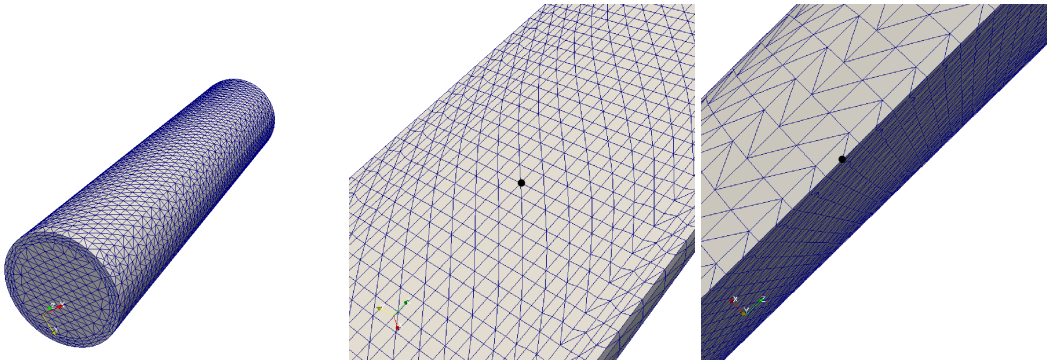

Fig. 1 A mesh of the FSI domain (left); selected point PtA indicated with a black dot (middle); selected point PtB indicated with a black dot (right).

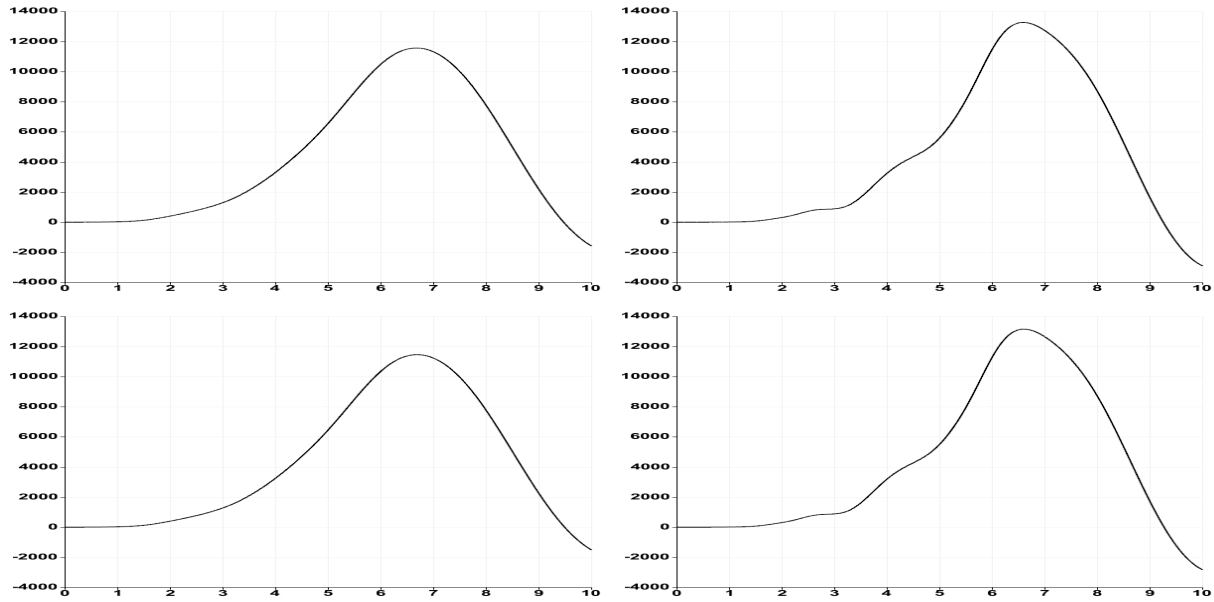

Fig. 2 Fluid pressure waves with $\beta = 0.5$, $\gamma = 1.0$ (first row); fluid pressure waves with $\beta = 0.625$, $\gamma = 1.0$ (second row). Fluid pressure waves at the point PtA (first column); fluid pressure waves at point PtB (second column).

in [64] does not behave well with respect to time discretization parameters which might lead to a violation of discrete $\inf - \sup$ conditions. As we discussed from the above, these two factors have been considered in this work. The fluid pressure waves obtained from the FSI simulation using the new stabilization parameter $\tau_{s,T}$, and proper choices of time discretization parameters β and γ, e.g., $\beta = 0.625$, $\gamma = 1.0$ and $\beta = 0.625$, $\gamma = 0.6$, are plotted in Fig. 3. It is observed that the wiggles are removed. From our numerical results, we suggest avoiding the choice of $\beta = 0.5$, $\gamma = 1.0$, where some wiggles are still visible.

A close look of fluid pressure waves at the points PtA and PtB is illustrated in Fig. 4. In each plot the fluid pressure waves using different choices of time discretization parameters, are compared with each other. From this comparison, we could see more clearly what we have drawn in the above.

6.2 FSI results with a two-layer structure model

In this example, we use a similar computational domain as for the case using a homogeneous structure model, except that the structure layer is split into an inner layer and an outer layer. As we pointed out at the beginning, the two-layer structure model we considered here is too simple to model real tissues in hemodynamics. However we believe this model is helpful to verify the methodology we have discussed. We also assume that the inner structure layer, Structure Layer 1 ($SL1$), has a compressible material ($\nu = 0.3003$), while the outer structure layer, Structure Layer 2 ($SL2$), has a nearly incompressible material ($\nu = 0.499999$). We only assume small jumps of densities and Young's modulus of $SL1$ and $SL2$ as specified in

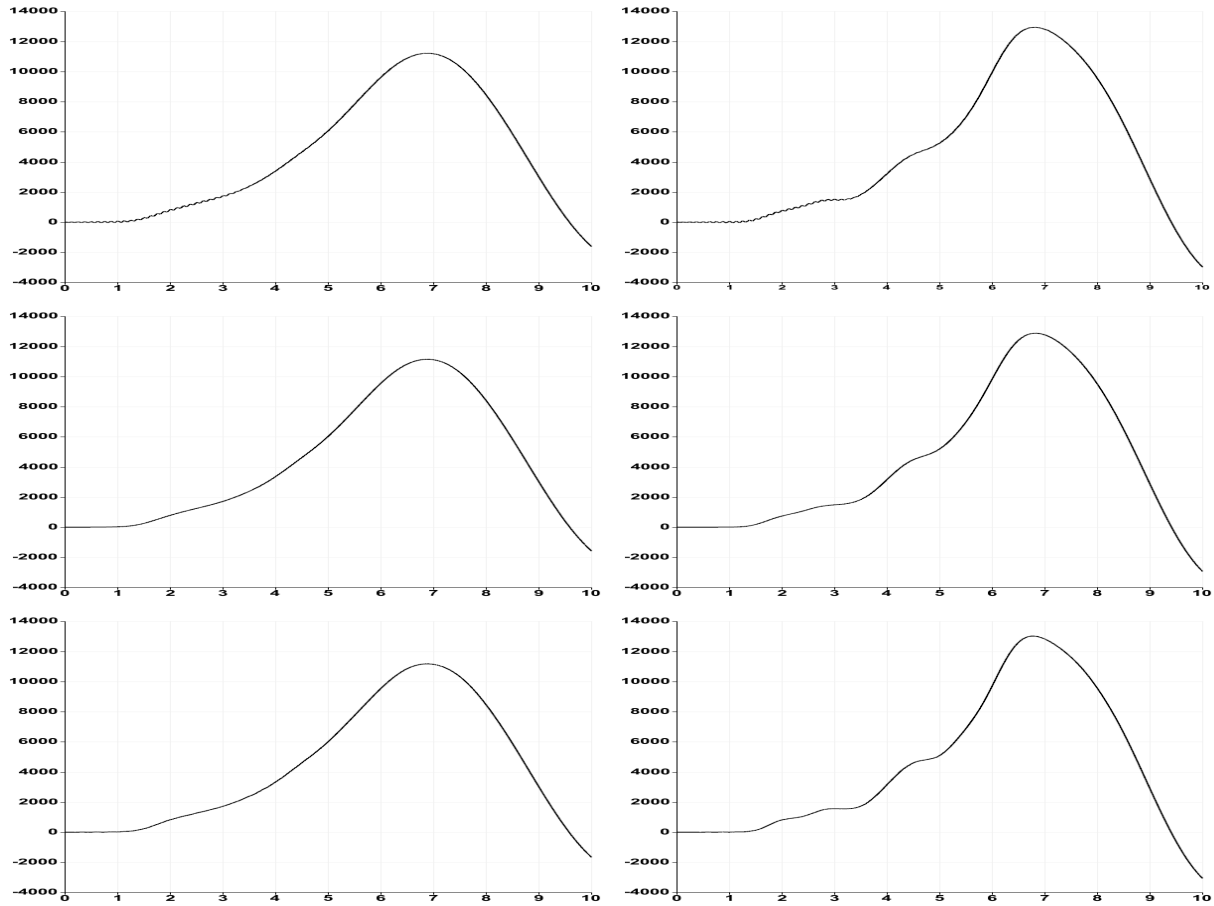

Fig. 3 Fluid pressure waves with $\beta = 0.5$, $\gamma = 1.0$ (first row); fluid pressure waves with $\beta = 0.625$, $\gamma = 1.0$ (second row); fluid pressure waves with $\beta = 0.625$, $\gamma = 0.6$ (third row). Fluid pressure waves at the point PtA (first column); fluid pressure waves at point PtB (second column).

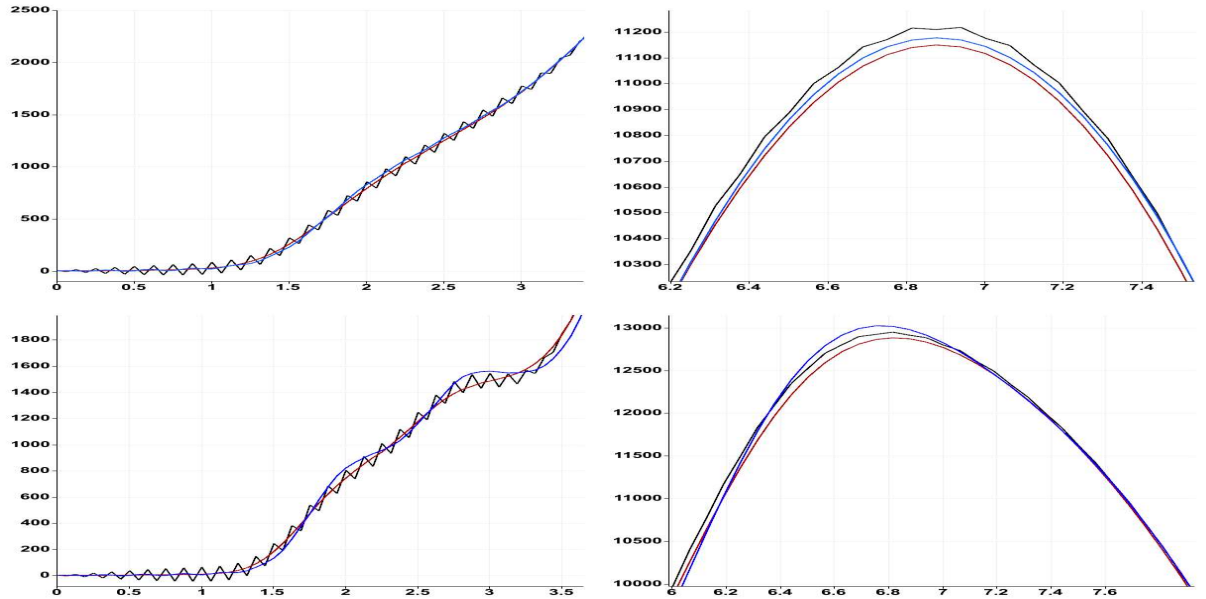

Fig. 4 Fluid pressure waves at the point PtA (first row) and at the point PtB (second row) using different time discretization parameters: $\beta = 0.5$, $\gamma = 1.0$ (black lines), $\beta = 0.625$, $\gamma = 1.0$ (red lines), $\beta = 0.625$, $\gamma = 0.6$ (blue lines). Fluid pressure waves at the early stage (first column); fluid pressure wave at the late stage (second column).

Table 2, since we restrict ourselves to FSI problems in hemodynamics. Note that only $SL1$ has a common interface with the fluid. Some other models with more complex computational domains are reported in [40, 63].

Fluid	Structure Layer 1	Structure Layer 2
$\rho_f = 1.0$ g/cm^3	$\rho_f = 1.2$ g/cm^3	$\rho_f = 1.4$ g/cm^3
$\mu = 0.03$ Poise	$E = 2.9908 \times 10^6$ dyn/cm^2	$E = 4.9908 \times 10^6$ dyn/cm^2
$g_{in} = (0, 0, 1.332 \times 10^4)^T$ dyn/cm^2 if $t \leq 3$ ms $g_{in} = 0$ dyn/cm^2 if $t > 3$ ms	$\nu = 0.3003$	$\nu = 0.499999$

Table 2 The values of fluid and two-layer structure material coefficients and fluid inflow boundary conditions.

We take different thicknesses of two layers. The thickness for $SL1$ is denoted by $TH1$, and for $SL2$ is denoted by $TH2$. We keep $TH1 + TH2 = 1$ mm, but vary each of them as listed in Table 3. The mesh contains 25428 nodes and 142546 tetrahedral elements (44388 elements for each structure layer and 53770 elements for the fluid). The total degrees of freedom is 101712. Besides two points PtA and PtB as we selected for recording the fluid pressure waves in the first

Thickness	Case I	Case II	Case III
$TH1$	0.25 mm	0.50 mm	0.75 mm
$TH2$	0.75 mm	0.50 mm	0.25 mm
$TH1 + TH2$	1.00 mm	1.0 mm	1.0 mm

Table 3 The variances of thicknesses of two structure layers.

numerical example, here another point PtC located on the surface between two structure layers is chosen as a sample point (which is also on the middle cutting plane orthogonal to z-direction); see Fig. 5 for an illustration. At the point PtC, we plot the structure pressure waves as functions of time t. The time step size is set as $\delta t = 0.015625$ ms, and we run the simulation until $t = 10$ ms in the following examples. We are interested in proper choices of time integration parameters β and γ, as well as in the sensitivities of numerical solutions with respect to varying thicknesses of two layers.

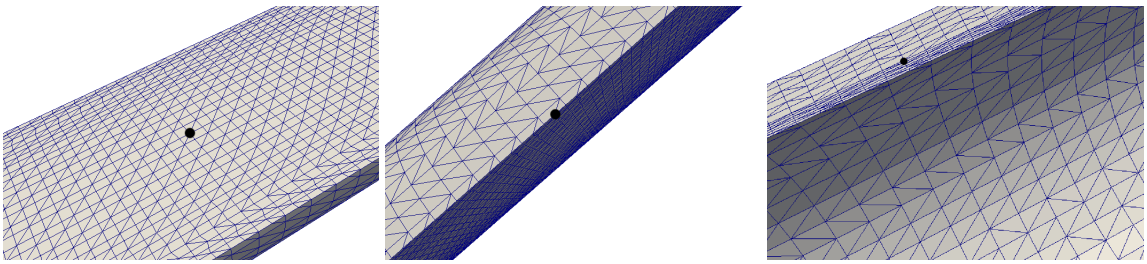

Fig. 5 An illustration of selected sample points indicated with black dots on the meshes: A point PtA at the middle of the center line of the fluid domain (left), a point PtB on the fluid-structure interface (middle), a point PtC on the surface of two structure layers (right).

In Case I, we consider a thinner $SL1$ ($TH1 = 0.25$ mm), and a little bit thicker $SL2$ ($TH2 = 0.75$ mm). The fluid pressure waves at the points PtA and PtB, the structure pressure waves at the point PtC are plotted in Fig. 6. Several issues have been observed from these numerical results. First of all, the numerical scheme becomes very sensitive to the choice of time discretization parameter β. For the choice of $\beta = 0.5$, strong oscillations of the fluid pressure waves at the points PtA and PtB, and the structure pressure wave at the point PtC, are developed after some wiggles appearing from previous time steps. Raising the value of β, we obtain more stable numerical solutions. This also conforms to what we have observed from the previous numerical example.

For Case II, we consider equal thickness for both layers $SL1$ and $SL2$: $TH1 = TH2 = 0.5$ mm. The fluid and the structure pressure waves are plotted in Fig. 7. The pressure waves using different values of time integration parameters are overlapping with each other. From the first glance, the numerical scheme becomes less sensitive compared with Case I. A close look of fluid pressure waves at the points PtA and PtB are plotted in Fig. 8. As we expected, some wiggles are still visible using the choice of time discretization parameters: $\beta = 0.5$, $\gamma = 1.0$. With the other two choices: $\beta = 0.625$, $\gamma = 1.0$ and $\beta = 0.725$, $\gamma = 1.0$, such wiggles have been smoothed out.

As opposed to Case I, we take a thicker $SL1$, $TH1 = 0.75$ mm and a thinner $SL2$, $TH2 = 0.25$ mm in Case III. The fluid and the structure pressure waves are plotted in Fig. 9, and a close look of the fluid pressure waves at the points PtA and PtB is plotted in Fig. 10. From these results, it is easy to see similar behavior of numerical solutions as in Case II, with respect to the choices of time integration parameters.

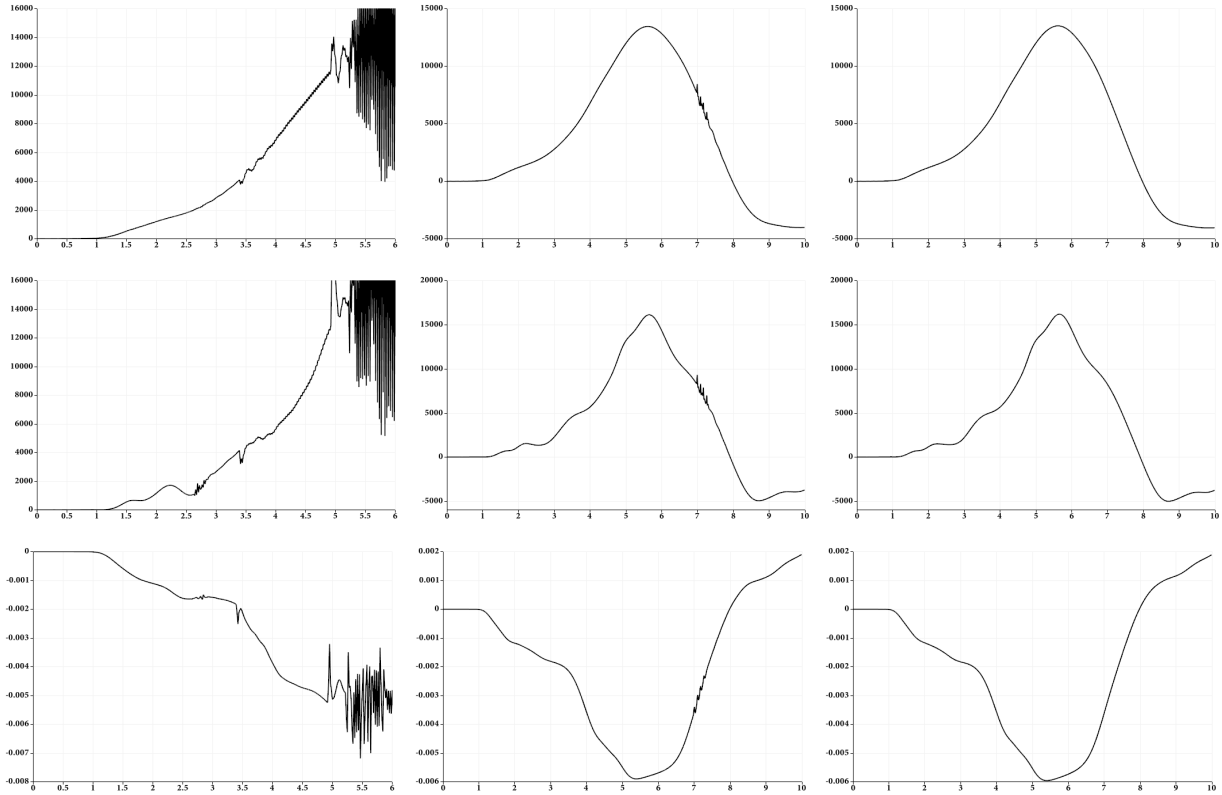

Fig. 6 Fluid pressure waves at the point PtA (first row) and at the point PtB (second row); structure pressure waves at the point PtC (third row). Different time discretization parameters: $\beta = 0.5$, $\gamma = 1.0$ (first column); $\beta = 0.625$, $\gamma = 1.0$ (second column); $\beta = 0.725$, $\gamma = 1.0$ (third column).

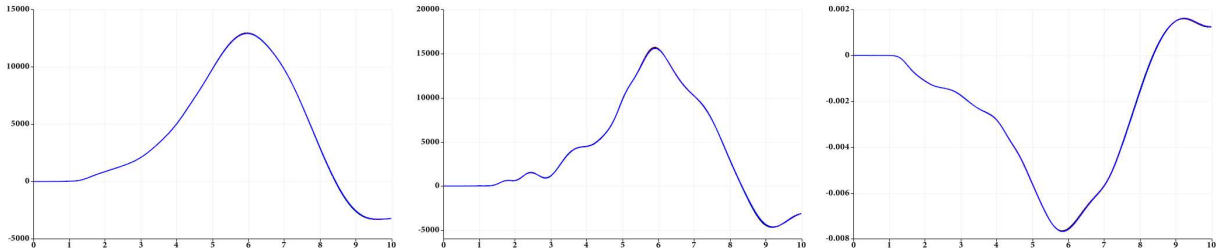

Fig. 7 Fluid pressure waves at the point PtA (left) and at the point PtB (middle); structure pressure waves at the point PtC(right). Different time discretization parameters: $\beta = 0.5$ (black lines), $\beta = 0.625$ (red lines), $\beta = 0.725$ (blue lines).

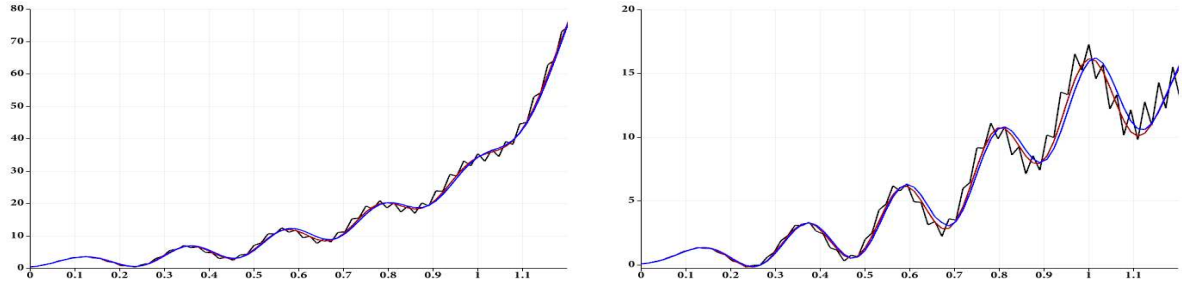

Fig. 8 A close look of fluid pressure waves at the point PtA (left) and at the point PtB (right). Different choices of time integration parameters: $\beta = 0.5$, $\gamma = 1.0$ (black lines); $\beta = 0.625$, $\gamma = 1.0$ (red lines); $\beta = 0.725$, $\gamma = 1.0$ (blue lines).

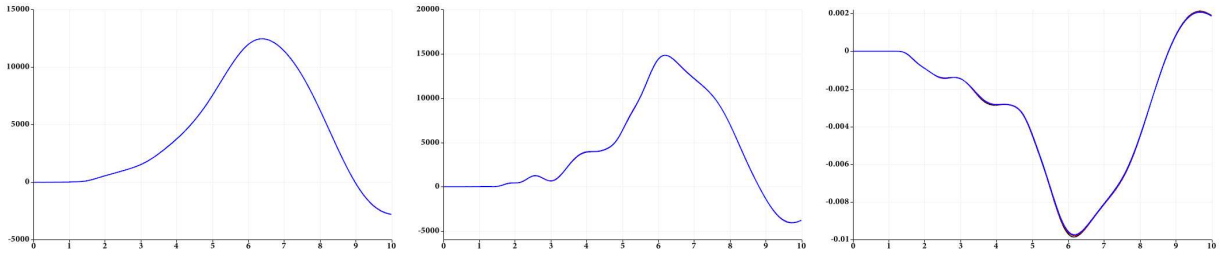

Fig. 9 Fluid pressure waves at the point PtA (left) and at the point PtB (middle); structure pressure waves at the point PtC (right). Different choices of time discretization parameters: $\beta = 0.5$, $\gamma = 1.0$ (black lines); $\beta = 0.625$, $\gamma = 1.0$ (red lines); $\beta = 0.725$, $\gamma = 1.0$ (blue lines).

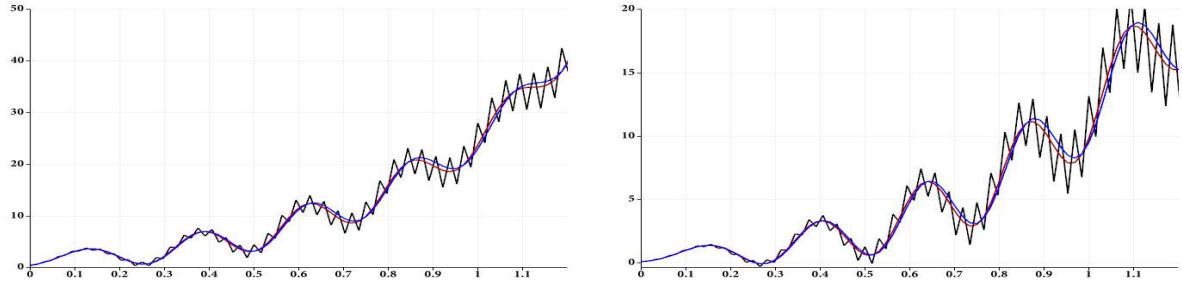

Fig. 10 A close look of fluid pressure waves at the point PtA (left) and at the point PtB (right). Different choices of time integration parameters: $\beta = 0.5$, $\gamma = 1.0$ (black lines); $\beta = 0.625$, $\gamma = 1.0$ (red lines); $\beta = 0.725$, $\gamma = 1.0$ (blue lines).

For this particular two-layer structure model with material parameters specified in Table 2, we also observe that the FSI solutions show some differences using the above three two-layer structure models. The numerical solutions, e.g., the fluid pressure waves at the point PtA, are plotted Fig. 11, where we use a time step size $\delta t = 0.015625$ ms, and choose the time integration parameters $\beta = 0.725$, $\gamma = 1.0$ for all three cases. It is easy to see that the thicker the inner layer, the faster the fluid pressure wave travels, and the lower wave peak it has.

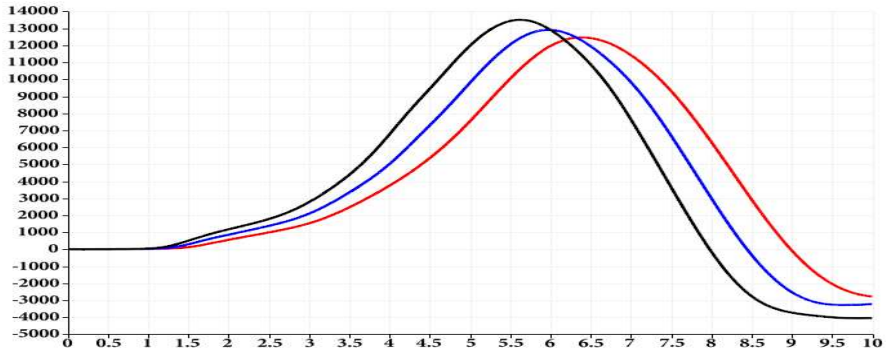

Fig. 11 Fluid pressure waves at the point PtA with three two-layer structure models: $TH1 = 0.25$ mm, $TH2 = 0.75$ mm (black line); $TH1 = 0.5$ mm, $TH2 = 0.5$ mm (blue line); $TH1 = 0.75$ mm, $TH2 = 0.25$ mm (red line).

6.3 Performance of the solvers

Performance for a class of partitioned FSI solvers as well as the AMG solvers for the homogeneous mixed elasticity models has been reported in [64]. In this section, we report the performance of the RN preconditioned GMRES solver as well as the AMG solver for the two-layer structure models. For measuring the performance, we test the FSI solvers on a laptop with an Intel Core of 2.67 GHz and 4 GB memory. For the RN preconditioned GMRES iteration (RN-GMRES-Iter), we use a relative residual reduction factor 10^{-6} of the Schur complement equation as a stopping criterion. For the fluid and the structure sub-problems, we only apply the AMG iteration (AMG-Iter) up to a relative residual reduction factor 10^{-2}

of the linear system. We choose $\beta = 0.725$ and $\gamma = 1.0$ for the time discretization parameters. For the Robin weighting parameter α_f, we first find an optimal choice by experimenting a simulation on a very coarse mesh. This value is used for the simulation on the fine mesh. For all the following tests, we use $\alpha_f = 4580$. We also test the performance with different time step sizes $\delta t = 0.0625$ ms, 0.03125 ms and 0.015625 ms.

Thickness		# RN-GMRES-Iter (Cost in second (s))		
$TH1$	$TH2$	$\delta t = 0.0625$ ms	$\delta t = 0.03125$ ms	$\delta t = 0.015625$ ms
0.25 mm	0.75 mm	6 (1428 s)	6 (1072 s)	6 (808 s)
0.50 mm	0.50 mm	7 (1304 s)	6 (898 s)	6 (681 s)
0.75 mm	0.25 mm	7 (1302 s)	6 (835 s)	6 (666 s)

Table 4 Number of iterations and cost of RN preconditioned GMRES solvers in each time step.

Thickness		# AMG-Iter (Cost in second (s))					
$TH1$	$TH2$	$\delta t = 0.0625$ ms		$\delta t = 0.03125$ ms		$\delta t = 0.015625$ ms	
		Dirichlet	Neumann	Dirichlet	Neumann	Dirichlet	Neumann
0.25 mm	0.75 mm	3 (33 s)	12 (130 s)	1 (10 s)	8 (87 s)	1 (11 s)	4 (44 s)
0.50 mm	0.50 mm	1 (11 s)	8 (89 s)	1 (11 s)	5 (55 s)	1 (11 s)	2 (22 s)
0.75 mm	0.25 mm	1 (11 s)	7 (77 s)	1 (11 s)	3 (33 s)	1 (11 s)	2 (22 s)

Table 5 Number of iterations and cost of AMG solvers for two-layer structure sub-problems.

As we see from Table 4, the iteration numbers of the RN preconditioned GMRES solver (# RN-GMRES-Iter) for all tests almost keep the same. The cost (indicated in the brackets and measured in second (s)) decreases when refining the time step size for each two-layer structure model. This is due to the factor that the cost for the structure sub-problems is decreasing. The cost for Case I is slightly higher compared with the other two cases, but still keeps in a reasonable range.

For the fluid sub-problem with the Robin boundary conditions that is required for the second step in the Gauss-Seidel iteration, the AMG solver needs about 2 iterations (10 s) for all test cases.

For solving the two-layer structure sub-problems, the number of AMG iterations (# AMG-Iter) and the cost are reported in Table 5. For solving the structure sub-problem with a prescribed Dirichlet boundary condition in the first step of the Gauss-Seidel iteration, it needs about 1 iteration for all cases. For solving the structure sub-problem with a prescribed Neumann boundary condition in the third step of the Gauss-Seidel iteration, about 2-12 iterations are required. The iteration numbers decrease with refined time step sizes, and the cost for Case I, is slightly higher than the other two cases.

7 Conclusions and future work

Proper choices of time integration parameters in the Newmark-β scheme combined with newly designed finite element stabilization parameters for the structure sub-problem have improved the robustness of the FSI solutions in both cases of homogeneous and nonhomogeneous structure models. Numerical experiments are confirmed with the theoretical analysis. For the particular FSI problems within two-layer composite vessels considered in this work, the RN preconditioned GMRES solver has shown its robustness and efficiency with respect to the time step size, the thicknesses of two layers, and the jumps of material coefficients. The special AMG solvers for both fluid and structure sub-problems also exhibit their high performance in terms of iteration numbers and the cost. In particular, for the two-layer structure sub-problem, it also demonstrates the robustness with respect to some material jumps. Although the stability of the mixed finite element discretization combined with the Newmark-β scheme has been shown, a rigorous numerical analysis on proper choices of time integration parameters β and γ is missing and will be considered in the future work. A more robust design of the least-square finite element discretization parameter $\tau_{s,T}$ with respect to a larger range of time step size is under an investigation. Another ongoing work is to replace currently used two-layer structure model by more realistic structure models, e.g., [32].

References

[1] R. A. Adams and J. J. F. Fournier. *Sobolev Spaces*, volume 140 of *Pure and Applied Mathematics*. Academic Press, Amsterdam, Boston, second edition, 2003.

[2] I. Babuška. The finite element method with Lagrangian multipliers. *Num. Math.*, 20:179–192, 1973.

[3] S. Badia and R. Codina. Analysis of a stabilized finite element approximation of the transient convection-diffusion equation using an ALE framework. *SIAM J. Numer. Aanl.*, 44(5):2159–2197, 2006.

[4] S. Badia, F. Nobile, and C. Vergara. Robin-Robin preconditioned Krylov methods for fluid-structure interaction problems. *Comput. Methods Appl. Mech. Engrg.*, 198:1768–2784, 2009.

[5] S. Badia, A. Quaini, and A. Quarteroni. Modular vs. non-modular preconditioners for fluid-structure systems with large added-mass effect. *Comput. Methods Appl. Mech. Engrg.*, 197(4950):4216 – 4232, 2008.

[6] A. Barker and X.-C. Cai. Scalable parallel methods for monolithic coupling in fluid-structure interaction with application to blood flow modeling. *J. Comput. Phys.*, 229:642–659, 2010.

[7] Y. Bazilevs, M.-C. Hsu, Y. Zhang, W. Wang, T. Kvamsdal, S. Hentschel, and J.G. Isaksen. Computational vascular fluid-structure interaction: methodology and application to cerebral aneurysms. *Biomech Model Mechanobiol*, 9:481–498, 2010.

[8] Y. Bazilevs, M.C. Hsu, Y. Zhang, W. Wang, X. Liang, T. Kvamsdal, R. Brekken, and J.G. Isaksen. A fully-coupled fluid-structure interaction simulation of cerebral aneurysms. *Comput. Mech.*, 46:3–16, 2010.

[9] B.F. Belgacem. The mortar finite element method with Lagrange multipliers. *Numerische Mathematik*, 84(2):173–197, 1999.

[10] M. Benzi and M.A. Olshanskii. An augmented Lagrangian-based approach to the Oseen problem. *SIAM J. Sci. Comput.*, 28(6):2095–2113, 2006.

[11] M. Benzi, M.A. Olshanskii, and Z. Wang. Modified augmented Lagrangian preconditioners for the incompressible Navier-Stokes equations. *Int. J. Numer. Meth. Fluids*, 66:486–508, 2011.

[12] D. Braess and R. Sarazin. An efficient smoother for the Stokes problem. *Appl. Numer. Math.*, 23:3–19, 1997.

[13] F. Brezzi. On the existence uniqueness and approximation of saddle-point problems arising from Lagrange multipliers. *RAIRO*, 2:129–151, 1974.

[14] F. Brezzi and M. Fortin. *Mixed and Hybrid Finite Element Methods*. Springer series in computational mathematics. Springer, New York, 1991.

[15] P. Causin, J. F. Gerbeau, and F. Nobile. Added-mass effect in the design of partitioned algorithm for fluid-structure problems. *Comp. Meth. Appl. Mech. Eng.*, 194:4506–4527, 2005.

[16] P. Crosetto, S. Deparis, G. Fourestey, and A. Quarteroni. Parallel algorithms for fluid-structure interaction problems in haemodynamics. *SIAM Journal on Scientific Computing*, 33(4):1598–1622, 2011.

[17] S. Deparis, M. Discacciati, G. Fourestey, and A. Quarteroni. Fluid-structure algorithms based on Steklov-Poincaré operators. *Comput. Methods Appl. Mech. Engrg.*, 195:5797–5812, 2006.

[18] J. Donea, A. Huerta, J.Ph. Ponthot, and A.R. Ferran. Arbitrary Lagrangian-Eulerian methods. In E. Stein, R.d. Borst, and T.J.R. Hughes, editors, *The Encyclopedia of Computational Mechanics*, volume 1, pages 413–437. Wiley& Sons, Ltd, 2004.

[19] H.C. Elman, D.J. Silvester, and A. J. Wathen. *Finite Elements and Fast Iterative Solvers with Applications in Incompressible Fluid Dynamics*. Oxford University Press, first edition, 2005.

[20] M. A. Fernández and M.Moubachir. A Newton method using exact Jacobians for solving fluid-structure coupling. *Comput. & Struct.*, 83(2-3):127–142, 2005.

[21] L. Formaggia and F. Nobile. A stability analysis for the arbitrary Lagrangian Eulerian formulation with finite elements. *East-West Journal of Numerical Mathematics*, 7:105–132, 1999.

[22] Ch. Förster. *Robust methods for fluid-structure interaction with stabilised finite elements*. PhD thesis, University Stuttgart, 2007.

[23] Ch. Förster, W.A. Wall, and E. Ramm. Stabilized finite element formulation for incompressible flow on distorted meshes. *International Journal for Numerical Methods in Fluids*, 60(10):1103–1126, 2009.

[24] Leopoldo P. Franca and R. Stenberg. Error analysis of some Galerkin least square methods for the elasticity equations. *SIAM Journal on Numerical Analysis*, 28(6):1680–1697, 1991.

[25] T. C. Gasser, R. W. Ogden, and G. A. Holzapfel. Hyperelastic modelling of arterial layers with distributed collagen fibre orientations. *J. R. Soc. Interface*, 3:15–35, 2006.

[26] M.W. Gee, U. Küttler, and W.A. Wall. Truly monolithic algebraic multigrid for fluid-structure interation. *Int. J. Numer. Meth. Engng.*, 85:987–1016, 2011.

[27] J.F. Gerbeau and M. Vidrascu. A Quasi-Newton algorithm based on a reduced model for fluid-structure interaction problems in blood flows. *ESAIM: Mathematical Modelling and Numerical Analysis*, 37(04):631–647, 2003.

[28] V. Girault and P.A. Raviart. *Finite Element Methods for Navier-Stokes Equations: Theory and Algorithms*. Springer, New York, 1985.

[29] W. Hackbusch. *Multi-Grid Methods and Applications*. Springer, 2010.

[30] S. Hamilton, M. Benzi, and E. Haber. New multigrid smoothers for the Oseen problem. *Numerical Linear Algebra with Applications*, 17(2-3):557–576, 2010.

[31] M. Heil. An efficient solver for the fully coupled solution of large-displacement fluid-structure interaction problems. *Comput. Methods Appl. Mech. Engrg.*, 193(1-2):1–23, 2004.

[32] G. A. Holzapfel, T. C. Gasser, and R. W. Ogden. A new constitutive framework for arterial wall mechanics and a comparative study of material models. *Jounral of Elasticity*, 61:1–48, 2000.

[33] T.J.R. Hughes, W.K. Liu, and T.K. Zimmermann. Lagrangian-Eulerian finite element formulation for incompressible viscous flows. *Comp. Meth. Appl. Mech. Eng.*, 29(3):329–349, 1981.

[34] J.D. Humphrey and G.A. Holzapfel. Mechanics, mechanobiology, and modeling of human abdominal aorta and aneurysms. *Journal of Biomechanics*, 45:805–814, 2012.

[35] D. Kay, D. Loghin, and A. Wathen. A preconditioner for the steady-state Navier-Stokes equations. *SIAM Journal on Scientific Computing*, 24(1):237–256, 2002.

[36] R.A. Khurram and A. Masud. A multiscale/stabilized formulation of the incompressible Navier-Stokes equations for moving boundary flows and fluid-structure interaction. *Comput. Mech.*, 38:403–416, 2006.

[37] F. Kickinger. Algebraic multigrid for discrete elliptic second-order problems. In *Multigrid Methods V. Proceedings of the 5th European Multigrid conference (ed. by W. Hackbush), Lecture Notes in Computational Sciences and Engineering, vol. 3*, pages 157–172. Springer, 1998.
[38] U. Küttler, M. Gee, Ch. Förster, A. Comerford, and W.A. Wall. Coupling strategies for biomedical fluid-structure interaction problems. *International Journal for Numerical Methods in Biomedical Engineering*, 26(3-4):305–321, 2010.
[39] U. Küttler and Wolfgang A. Wall. Fixed-point fluid-structure interaction solvers with dynamic relaxation. *Comput. Mech.*, 43:61–72, 2008.
[40] U. Langer and H. Yang. Domain decomposition solvers for some fluid-structure interaction problems. *PAMM*, 12(1):375–376, 2012.
[41] M.Heil, A.L. Hazel, and J. Boyle. Solvers for large-displacement fluid–structure interaction problems: segregated versus monolithic approaches. *Comput. Mech.*, 43:91–101, 2008.
[42] D.S. Molony, A. Callanan, E.G. Kavanagh, M.T. Walsh, and T.M. McGloughlin. Fluid-structure interaction of a patient-specific abdominal aortic aneurysm treated with an endovascular stent-graft. *BioMedical Engineering OnLine*, 8:24, 2009. doi:10.1186/1475-925X-8-24.
[43] R.L. Muddle, M. Mihajlović, and M. Heil. An efficient preconditioner for monolithically-coupled large-displacement fluid-structure interaction problems with pseudo-solid mesh updates. *Journal of Comput. Phys.*, 231(21):7315 – 7334, 2012.
[44] N.M. Newmark. A method of computation for structural dynamics. *Journal of Engineering Mechanics*, 85 (EM3):67–94, 1959.
[45] M.A. Olshanskii and A. Reusken. Navier-Stokes equations in rotation form: A robust multigrid solver for the velocity problem. *SIAM J. Sci. Comput.*, 23(5):1683–1706, 2001.
[46] A. Quarteroni and A. Valli. *Domain Decomposition Methods for Partial Differential Equations*. Oxford Science Publications, Oxford, 1999.
[47] M. Razzaq, H. Damanik, J. Hron, A. Ouazzi, and S. Turek. FEM multigrid techniques for fluid-structure interaction with application to hemodynamics. *Appl. Numer. Math.*, 62(9):1156–1170.
[48] Y. Saad and M. H. Schultz. Gmres : A generalized minimal residual algorithm for solving nonsymmetric linear system. *SIAM J. Sci. Stat. Comput.*, 7:856–869, 1986.
[49] C.M. Scotti, A.D. Shkolnik, S.C. Muluk, and E.A. Finol. Fluid-structure interaction in abdominal aortic aneurysms: effects of asymmetry and wall thickness. *BioMedical Engineering OnLine*, 4:64, 2005. doi:10.1186/1475-925X-4-64.
[50] A. Toseli and O. Widlund. *Domain Decomposition Methods - Algorithms and Theory*. Springer, Oxford, 2004.
[51] U. Trottenberg, C. Oosterlee, and A. Schüller. *Multigrid*. Academic Press, first edition, 2000.
[52] S. Turek. *Efficient Solvers for Incompressible Flow Problems*. Springer, Berlin, first edition, 1999.
[53] H.A. van der Vorst. BI-CGSTAB: a fast and smoothly converging variant of BI-CG for the solution of nonsymmetric linear systems. *SIAM J. Sci. Stat. Comput.*, 13(2):631–644, 1992.
[54] R. Verfürth. Error estimates for a mixed finite element approximation of the Stokes equations. *R.A.I.R.O. Num. Anal.*, 18(2):175–182, 1984.
[55] M. Wabro. *Algebraic Multigrid Methods for the Numerical Solution of the Incompressible Navier-Stokes Equations*. PhD thesis, Johannes Kepler University Linz, 2003.
[56] M. Wabro. Coupled algebraic multigrid methods for the Oseen problem. *Comput. Vis. Sci.*, 7:141–151, 2004.
[57] M. Wabro. AMGe—coarsening strategies and application to the Oseen equations. *SIAM J. Sci. Comput.*, 27:2077–2097, 2006.
[58] Wolfgang A. Wall. *Fluid-Struktur-Interaktion mit stabilisierten Finiten Elementen*. PhD thesis, Universität Stuttgart, 1999.
[59] D.H. Wang, M. Makaroun, M.W. Webster, and D.A. Vorp. Mechanical properties and microstructure of intraluminal thrombus from abdominal aortic aneurysm. *Journal of Biomechanical Engineering*, 123:536–539, 2001.
[60] T. Washio, T. Hisada, H. Watanabe, and T.E. Tezduyar. A robust preconditioner for fluid-structure interaction problems. *Comput. Methods Appl. Mech. Engrg.*, 194(3941):4027–4047, 2005.
[61] Barbara I. Wohlmuth. A mortar finite element method using dual spaces for the lagrange multiplier. *SIAM Journal on Numerical Analysis*, 38(3):989–1012, 2001.
[62] H. Yang. *Numerical Simulation of Fluid-Structure Interaction Problems on Hybrid Meshes with Algebraic Multigrid Methods*. PhD thesis, Johannes Kepler University Linz, 2010.
[63] H. Yang. Domain decomposition solvers for the fluid-structure interaction problems with anisotropic elasticity models. Technical Report 2012-11, RICAM, 2012.
[64] H. Yang. Partitioned solvers for the fluid-structure interaction problems with a nearly incompressible elasticity model. *Computing and Visualization in Science*, 14:227–247, 2012.
[65] H. Yang and W. Zulehner. Numerical simulation of fluid-structure interaction problems on hybrid meshes with algebraic multigrid methods. *Journal of Computational and Applied Mathematics*, 235:5367–5379, 2011.
[66] W. Zulehner. A class of smoothers for saddle point problems. *Computing*, 65:227–246, 2000.